Design and Characterization of Self-Biasing NiTi Spring Actuator

by

Apratim Chakraborty

A thesis
presented to the University of Waterloo
in fulfillment of the
thesis requirement for the degree of
Master of Applied Science
in
Mechanical Engineering

Waterloo, Ontario, Canada, 2016

Author's Declaration

I hereby declare that I am the sole author of this thesis. This is a true copy of the thesis, including any required final revisions, as accepted by my examiners.

I understand that my thesis may be made electronically available to the public.

Abstract

Spring actuators are essential components in vehicles as they are used for climate control, braking ventilation, engine control and fuel management. However, commercially available spring actuators are heavy and expensive and need to be replaced by lower-weight SMA spring actuators. Potential applications of the particularly promising NiTi shape memory alloys (SMA) in automotive spring actuators is currently limited due to low awareness. Recently, laser processing has been used to make processing monolithic NiTi wires more flexible than ever by locally changing the wire composition to achieve multiple functional properties. Using laser-processing to add multiple memories in a monolithic NiTi spring wire would allow for the fabrication of a novel self-biasing spring actuator which would lead to lower equipment costs, reduced weight and enhanced flexibility. To obtain a successful self-biasing spring, processing and spring fabrication techniques for NiTi wires need to be studied.

The first part of the study involved investigating the effect of incrementing the number of laser pulses per spot and post-processing heat treatment temperatures on the composition of Ni-49.2 at.% Ti SMA wires. This was achieved by performing Differential Scanning Calorimetry (DSC) analysis and observing the shift in phase transformation temperatures. Results revealed that increasing the number of laser pulses increased the transformation temperatures up to a point at which the samples become Ti-rich and there is negligible effect on composition. Heat treatment study showed that heat treatment temperature had a significant impact on the transformation temperature peaks resulting in distinct peaks for base material and laser-processed samples. Mechanical properties of different heat-treated samples were examined using tensile test plots to determine the optimal heat treatment temperature for shape-setting springs.

In the second part of the study, the effect of spring geometry on spring force and the effect of incorporating multiple memory in a spring actuator was studied. A unique spring-shape setting fixture was used to fabricate springs with consistent spring pitch and diameter. Results showed that increasing the spring pitch and decreasing the mean coil diameter increased the spring force, which conforms to the established spring force equation. Incorporating multiple memories in a monolithic spring enabled thermally-induced self-biasing spring actuation due to various austenitic transformation temperatures triggering unique functional properties.

Acknowledgements

I would like to thank my supervisor, Dr. Mustafa Yavuz, for his timely guidance and support during my research. I would not have had the confidence to pursue grad studies if not for his invaluable advice to help me excel in life and academics.

I would also like to extend my thanks to Andrew Michael who helped me immensely with my MASc research. Without his guidance, I would not have been able to present my thesis in time. He was a constant presence and motivator during challenging times in my research. In addition, he helped me write my first journal paper, pending acceptance, and reviewed my thesis.

I would like to thank Professor Norman Zhou, Dr. Ibraheem Khan (CEO of Smarter Alloys©) and all members of Smarter Alloys who helped me get started with my research on shape memory alloys.

Special thanks to Mark Griffett, lab technician at the materials lab, with whom I spent countless hours wire-drawing samples. Without the swift and efficient work of the Engineering Machine Shop (EMS), I wouldn't have been able to get my setups made in time, so a huge thank you to Mark and Rick for attending to my needs. I had a great time learning how to machine at the Engineering Student Machine Shop (ESMS) thanks to the approachability and friendliness of technicians Graeme and Andrew.

My friends at University of Waterloo, including colleagues from Center of Advanced Joining (CAMJ) were instrumental to me integrating into graduate-study life. Also, I would like to thank my colleague Greg for helping me make the test setup for the self-biased spring.

Finally and most importantly, I would like to thank my family for their patience and support during the course of my MASc research.

Dedication

To My Loving Parents for their Unwavering Support,
My One-of-a-kind Charismatic Younger Brother for his Patience,
&
Brotherly Andrew for Sacrificing Family Time to Help Me

Table of Contents

List of Figures

List of Tables

List of Equations

Chapter 1

1 Introduction

Ever since Beuhler et al. discovered NiTi (nickel-titanium alloy) in 1963 [1], shape memory alloys (SMA) have paved their way into numerous applications in medical, aerospace, microelectronics and automotive industries [2]. The use of NiTi springs as actuators in vehicles has been well documented in literature [2-4]. Commercially available springs, made using various types of steel, are widely used due to their usability and sustainability. NiTi springs made commercially are not as widely used due to lack of sufficient knowledge about optimizing material's properties to suit the needs of current applications in automotive industries. That combined with little engineering data and low awareness of SMA-based actuators has hindered the industrial success of NiTi spring actuators. However, the knowledge barrier can be overcome by studying more about materials known as "Smart Materials".

"Smart Materials" such as shape memory alloys are unique because they have two distinct properties, namely pseudoelasticity (PE) and shape memory effect (SME). Pseudoelasticity allows SMAs to recover large amounts of strain (approximately 8 % in polycrystalline materials), whereas SME allows an SMA to recover its original shape using thermal energy. These properties enable SMAs to achieve various mechanical and thermal properties for use in different applications in industry [2]. SMAs can be trained to perform different functions and their properties can be maneuvered with more precision compared to regular metallic alloys.

Due to this controllability, NiTi SMAs are tantalizing candidates to replace steel as the main material in spring actuators. This thesis demonstrates the conversion of commercially available monolithic NiTi SMA wires to self-biased spring actuators, which could potentially replace present-day steel spring actuators used in modern cars.

1.1 Motivation

Actuators are devices which convert mechanical, electrical or thermal energy into motion. Vehicles consist of 100 or more actuators which are used to control engine, transmission and suspension performance, to improve safety and reliability and enhance driver comfort. Existing

actuators used in automobiles are heavy and expensive [3]. They need to be replaced by self-biasing NiTi spring actuators because (1) in spring actuators, the maximum stroke and recovery force is much higher [5] than that of a linear actuator, (2) NiTi spring actuators provide higher work output at lower weights compared to other actuators used for automobiles [5] (for more details, see **section 2.5.2**), and (3) monolithic NiTi self-biasing spring actuator eliminates the use of a biasing spring, lowering equipment costs. To optimize the performance of self-biased NiTi spring actuators, comprehensive analysis between laser parameters and spring properties is required.

1.2 Objectives

To fabricate a self-biasing spring actuator, a detailed investigation of spring characteristics (such as diameter and pitch) and laser processing parameters is required. The goal of the current thesis is to determine a matrix of parameters to achieve optimal self-biased actuation:

- Determine number of pulses required for laser processing NiTi wire and allowing desired shift in transformation temperatures.
- Optimize heat treatment parameters for a self-biased NiTi spring actuator.
- Characterize mechanical properties of self-biased NiTi spring

1.3 Thesis Organization

The present work studies the effect of laser processing and changing spring parameters on NiTi springs for use in NiTi self-biased spring actuator. Chapter 2 provides a brief overview of NiTi shape memory alloys, laser processing and spring actuators. The experimental setup is presented in Chapter 3. Chapter 4 investigates the effect of heat treatment and laser pulses on the thermal and mechanical properties of NiTi springs. Spring geometry and self-biasing spring actuator characterization is presented in Chapter 5. Finally, conclusions and recommendations for future work is provided in Chapter 6.

Chapter 2

2 NiTi Shape Memory Spring Fundamentals

2.1 Shape Memory Alloys

The study of designing a NiTi self-biasing spring actuator requires a comprehensive understanding of NiTi Shape Memory Alloys. Fundamentals such as NiTi microstructure, phase transformation kinetics and various manufacturing techniques need to be studied to recognize the effect they have on material properties.

2.1.1 Description and Phases

2.1.1.1 Definition

A shape memory alloy (SMA) is a type of alloy which is distinguished by two unique properties namely shape memory effect (SME) and pseudoelasticity (PE). Various types of shape memory alloys commonly used are Nickel Titanium (NiTi), Copper-Zinc-Aluminium (Cu-Zn-Al), Cu-Ni-Ti and Cu-Al-Ni. Typically, NiTi alloys are preferred over other SMAs due to their superior ductility, strength, recoverable strains, corrosion resistance and stability of transformation temperatures [6]. For this thesis, binary NiTi alloy is used as the SMA for the self-biasing spring actuator because it is simpler and has more familiar material properties compared to ternary NiTi alloys such as Cu-Ni-Ti

2.1.1.2 Phases and Phase Transformations

Phases are regions of space within a material wherein all physical properties of the material are uniform. SMAs have three distinct phases namely martensite, austenite and rhombohedral (R) phases as illustrated in **Figure 2-1** below. Martensite is a low-temperature phase, which resembles a monoclinic B19' crystal structure with lattice parameters a = 0.2889, b = 0.4120 and c = 0.4622 and monoclinic angle $\beta = 96.8°$ [7]. At low temperatures, martensite can have two distinct microstructures known as twinned and detwinned martensite which will be discussed shortly (see **section 2.1.2: Twinning in Martensitic NiTi**). Conversely, austenite, also known as B2 austenite, is a high-temperature phase with a simple cubic Cs-Cl type crystal structure. Rhombohedral (R) phase, as the name suggests, has a rhombohedral crystal structure which helps accommodate a

small amount of strain during transformation of B2 austenite to B19' martensite. R-phase in NiTi is generally introduced during cold-working due to the formation of precipitates [8].

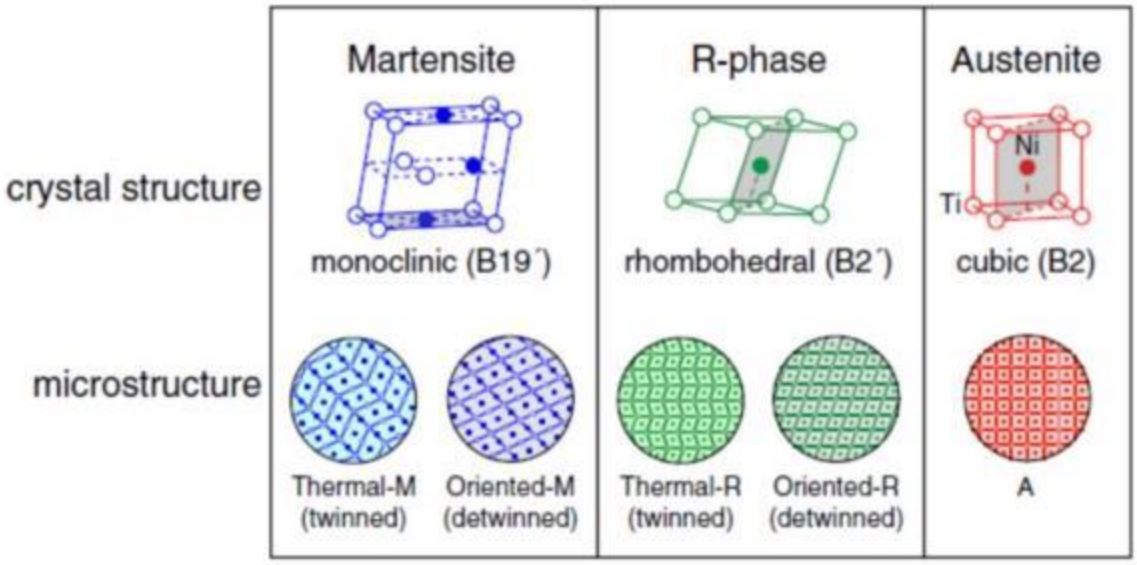

Figure 2-1: Three Distinct Phases of NiTi SMA: (a) monoclinic B19' martensite, (b) rhombohedral B2' R-phase and (c) cubic B2 austenite phase [9].

Phase transformations occur when NiTi is subjected to external stimulus such as heat or applied stress. For instance, martensitic transformations from B2 austenite to B19' martensite occur when NiTi is cooled below the austenite ⇌ martensite transformation temperature range (TTR). Similarly, austenitic transformations are triggered when NiTi is heated above TTR. TTR varies from 100 °C to well below liquid nitrogen temperature (boiling point -195.8 °C) depending on alloying composition of binary and ternary NiTi alloys [10]. Ternary alloying with cobalt, iron, vanadium, copper and aluminium are well known. CuNiTi is usually used to improve corrosion resistance of NiTi alloys.

2.1.2 Twinning in Martensitic NiTi

Twinning is the formation of a mirrored structure due to atomic displacement across a particular plane in a crystal structure [10]. In NiTi, twinning allows accommodation of strain during thermally-induced martensitic transformation. Twinning occurs due to a lack of symmetry and available slip systems at the atomic level. This results in a change of shape but no change of volume occurs at the macroscopic level [7].

Compared to steel, where slipping at the atomic level is the dominant mechanism during thermally-induced martensitic transformation, NiTi undergoes a recoverable twinning process from B2 austenite to twinned B19' martensite, which allows for accommodation of externally applied stress. NiTi detwins in response to applied stress by reorienting its twinned lattice structure [11]. This is possible because no bonds are broken during detwinning and therefore the twins have low energy and high mobility.

2.1.3 Shape Memory Effect

For NiTi SMAs, shape memory effect occurs when thermally-induced twinned B19' martensitic NiTi is put under applied stress to form detwinned martensite, which is then heated above the TTR to form the parent B2 austenite NiTi structure, and as it cools down below the TTR, the lattice structure reorients itself to go back to the initial twinned martensitic structure as shown in **Figure 2-2**. Shape recovery occurs at the austenite phase because it is symmetrical with a single variant. Martensitic NiTi, on the other hand, has 24 variants, but change of shape during martensitic transformation cannot be observed at a macroscopic level at room temperature [10].

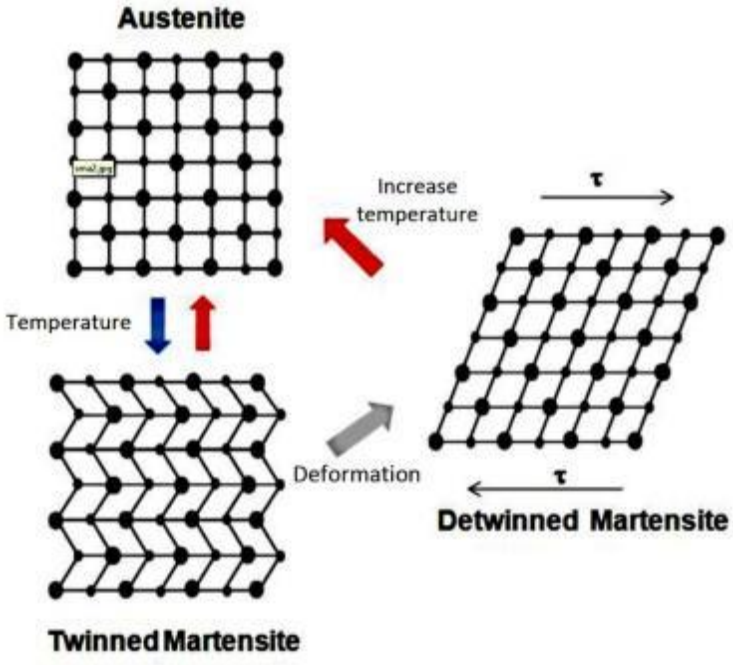

Figure 2-2: Illustration of Shape Memory Effect in NiTi SMA [12].

At the macroscopic level, as shown in **Figure 2-3**, change of shape in NiTi macrostructure occurs

during detwinning from twinned to detwinned martensite when external stress is applied and from detwinned to austenitic martensite when heat is applied. Shapes can be programmed into the NiTi SMA using a technique called shape-setting, which involves fixing shape, heat-treating at a temperature range of 325-525°C for 5-30 minutes, followed by a water quench to stabilize the NiTi structure to the fixed shape [13].

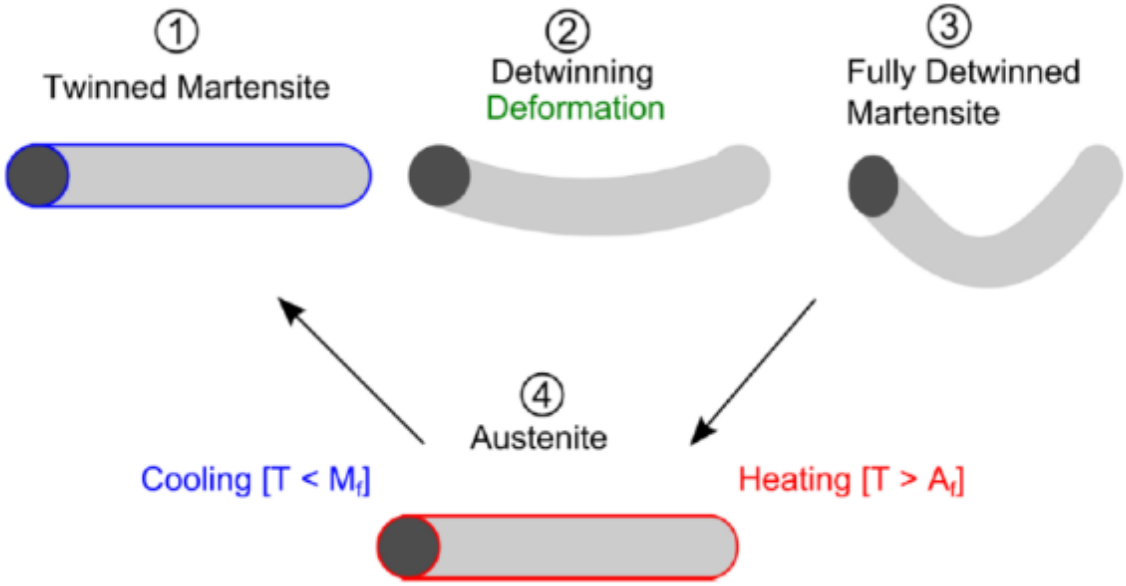

Figure 2-3: Shape memory effect illustrated at the macroscopic level [14].

The phase transformations shown in **Figure 2-2** can be thermally characterized using a method called Digital Scanning Calorimetry (DSC) which helps determine four specific transformation temperatures: austenite start (As), austenite finish (Af), martensite start (Ms), and martensite finish (Mf), as shown in **Figure 2-4**. The DSC plot shows that martensitic NiTi completely converts to austenitic NiTi above A_f, and complete austenitic to martensitic NiTi phase transformation occurs below M_f. A_s and M_s indicate the transformation temperatures at which NiTi starts changing phase from martensite to austenite and, from austenite to martensite respectively.

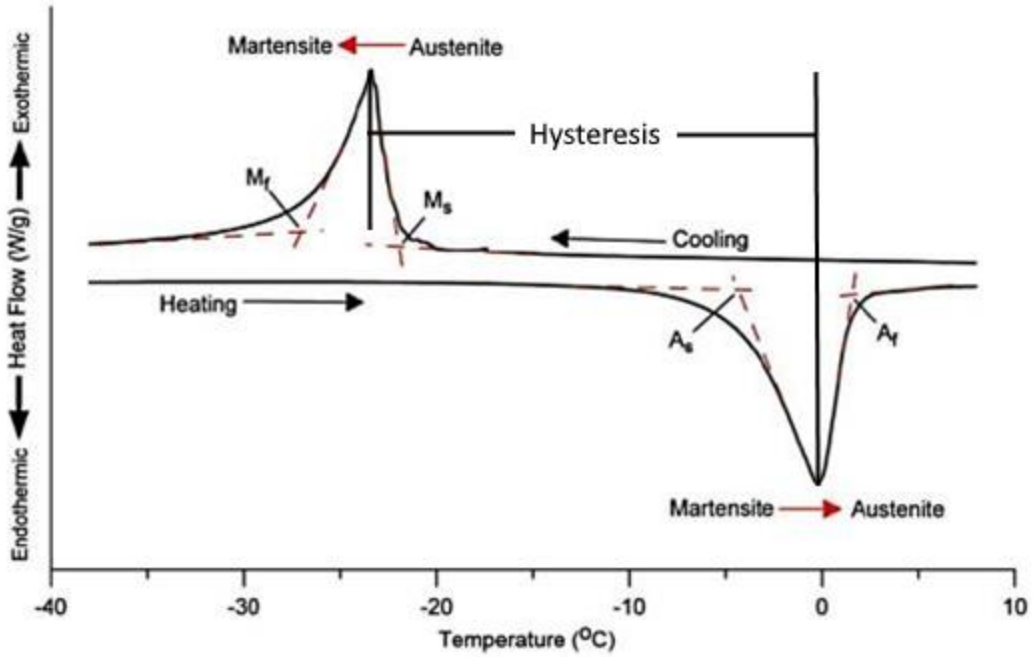

Figure 2-4: Typical DSC curve of NiTi SMA [15].

Furthermore, a distinct hysteresis between martensite peak (M_p) and austenite peak temperature (A_p) is observed in the DSC plot in **Figure 2-4**. This occurs due to frictional forces encountered during the lattice movements across interfaces and defects [10]. The magnitude of this hysteresis is typically between 10 °C to 50 °C, depending on the composition, processing and stress state of the material [16-18]. However, there is limited plastic deformation during transformation, which maintains coherency between phases and enables them to expand and contract depending on the thermodynamics of the system [15, 19]. On the contrary, martensitic formation of steel is not reversible because of large volume change between processes (as observed in **Table 2-1**) which results in large plastic strains [20].

Table 2-1: Percent volume change between austenite and martensite [15].

Alloy	**NiTi**	**CuAlNi**	**FeNiC Alloy**
%vol. change	0.023	0.297	-2.586

2.1.4 Pseudoelasticity

Another significant property of NiTi SMA, termed pseudoelasticity, is observed when mechanical stress is applied to transform parent B2 austenite phase into stress-induced martensite (SIM). The mechanical response is similar to detwinning of martensite. When pseudoelastic NiTi is pulled to failure, the stress-strain curve in **Figure 2-5** is obtained. In region (1), the material is initially in the parent austenite phase and it elastically deforms until it reaches critical stress, σ_{SIM}. Beyond this point, the strain keeps increasing while the stress remains constant, slightly below σ_{SIM}, as austenite transforms to SIM in region (2). A plateau is observed in this region because austenite is gradually consumed to form SIM, and at the end of region 2, all of the parent phase is consumed.

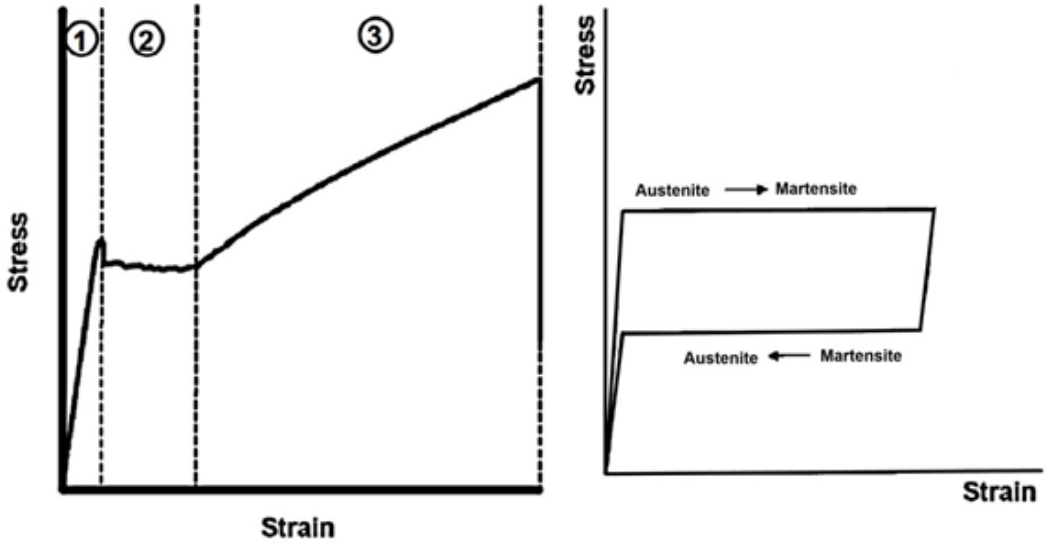

Figure 2-5: Stress-strain curve of pseudoelastic NiTi, when (a) pulled to failure, (b) load is released in region (2). Adapted from [21].

Further straining beyond region (2) results in an elastic then plastic deformation of detwinned martensite in region (3), which complies with Hooke's law. Removing stress in region (2) results in a reversible transformation (see **Figure 2-5 (b)**) at lower stress (σ_r) due to transformational hysteresis [22], similar to thermal hysteresis associated with SME.

Functional properties of NiTi are determined by the stable phase at the working temperature. SME is formed below M_f, while PE is observed above A_f but below the martensite deformation temperature (M_d) as shown in **Figure 2-6**. M_d is the highest temperature that martensite can form from austenite as a result of applied stress. The stress-temperature conditions shown in **Figure 2-6**

indicate that SME and PE coexist between temperatures M_s and M_f, and A_s and A_f respectively because the transformation is incomplete.

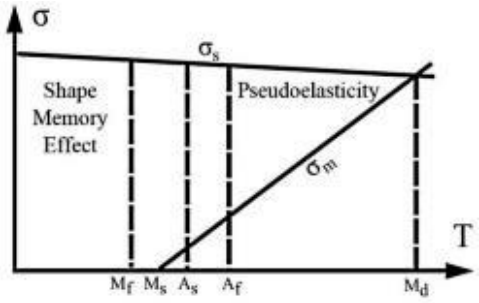

Figure 2-6: Stress-temperature conditions for NiTi SMAs exhibiting shape memory effect and pseudoelasticity [23].

As the temperature of NiTi increases above A_f, the thermodynamic stability of austenite phase also increases, which results in parallel increase of σ_{SIM} as shown in **Figure 2-7**. The linear relationship between tensile stress and temperature is derived from the Clausius-Clapeyron equation shown below [24]:

$$\frac{d\sigma}{dT} = \frac{-\Delta H}{T\varepsilon_t} \tag{2-1}$$

The symbol $d\sigma$ denotes the change in σ_{SIM}, dT is the change in test temperature, ΔH is the latent heat of transformation and ε_t is the transformational strain. The left-side of **Equation (2-1)** indicates the stress-rate which varies from 3 to 20 MPa/°C, depending on the material's processing history [24]. At temperatures above M_d, the specimen fails before the onset of PE.

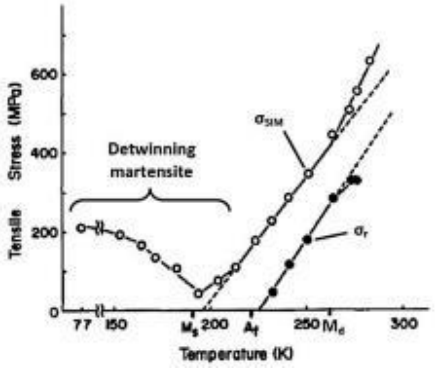

Figure 2-7: Plateau stress versus temperature plot. Dashed lines represent linear Clausius-Clapeyron relation between σ_{SIM} (empty circles), σ_r (filled circles) and temperature when $T>A_f$. Martensite detwinning occurs below A_f and plastic deformation of austenite occurs above M_d causing deviations from Clausius-Clapeyron relationship [25].

2.1.5 Physical Metallurgy and NiTi Composition

Composition of NiTi determines the thermomechanical properties it will exhibit. NiTi SMAs are considered stoichiometric intermetallic compounds (IMCs) [26] with an equiatomic or near-equiatomic distribution of Nickel and Titanium. At room temperature, the constituent species of NiTi are immiscible; heat treatment performed between 300 to 600 °C results in formation of Ni-rich metastable intermetallic compounds (IMCs) such as Ti_3Ni_4 and Ti_2Ni_3 as shown in **Figure 2-8**, and; above 650 °C, Ni-rich SMAs can be formed through quenching [27]. While NiTi is the only IMC known to retain SMA properties, precipitation of other Ni-rich IMCs can be used to modify these properties [11].

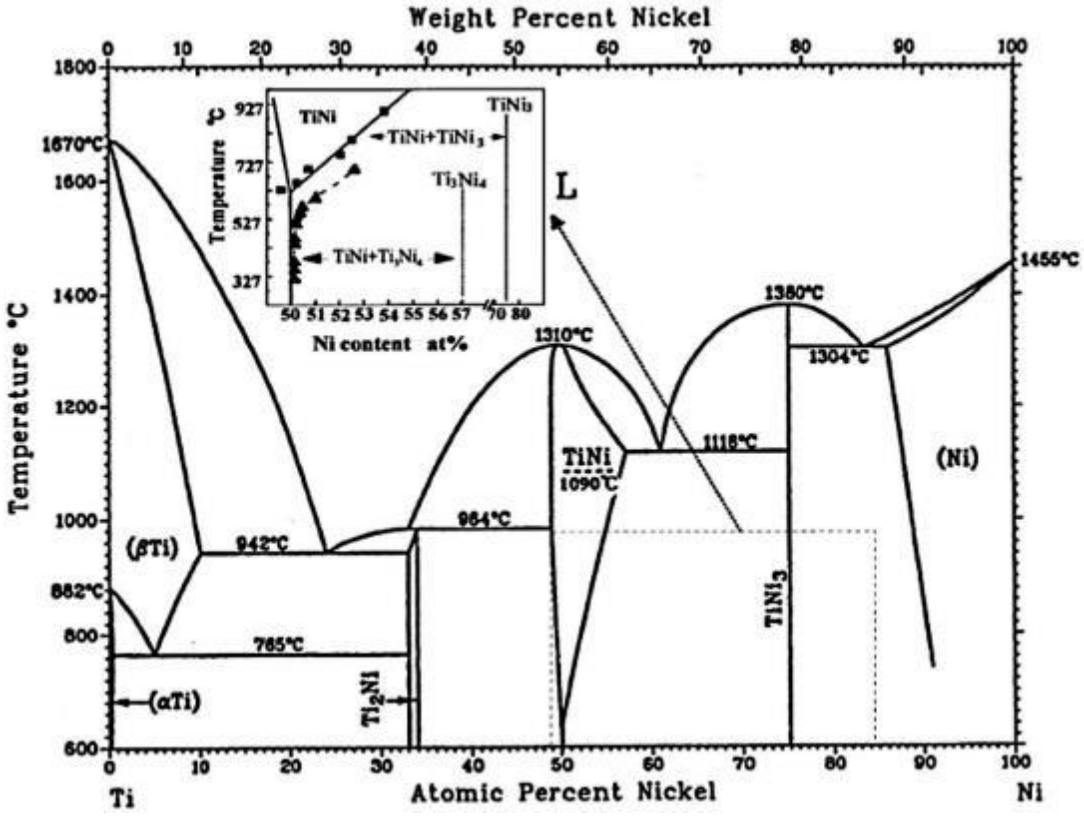

Figure 2-8: Binary Ti-Ni phase diagram [26].

In 1997, Tang showed that transformation temperature is heavily dependent on mole-fraction of Ni in NiTi. From 50 at.% up to around 51 at.%, there is a sharp decrease in transformation temperature as shown in **Figure 2-9**. At about 65 °C (approximately 338 K), the transformation temperature stays constant as Ni at.% decreases due to insolubility of Ti below 50 at.% Ni (see **Figure 2-8**).

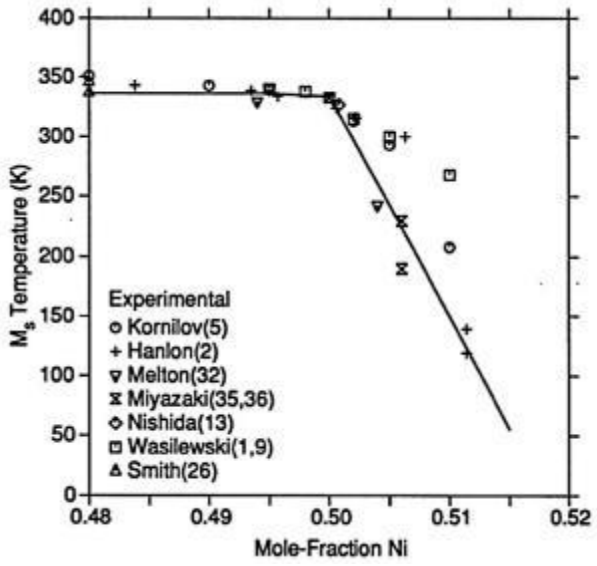

Figure 2-9: Relationship between mole-fraction of Ni and the M_s temperature in binary NiTi SMAs [28].

In addition to change in transformation temperature, altering composition affects the amount of stress required to form SIM, since a lower A_f is linked with a more stable austenite phase [29]. Therefore, precise control of composition is critical to achieve desired thermal and mechanical properties. Typically, composition tolerance for commercial NiTi is 0.05 at. % or ±5 °C [30].

2.2 Manufacturing NiTi

To obtain the desired functional properties, it is critical to know and understand the manufacturing process involved to produce NiTi. Commercially-available NiTi SMAs are produced with different material composition and properties as specified by the manufacturer, but these properties can vary based on the manufacturing technique used.

2.2.1 Refining, Casting and Powder Metallurgy

Ni and Ti do not occur naturally in their regular metallic form. Instead, they are extracted in mineral-form from ores such as limonite, garnierite and pentlandite for Ni, and rutile, ilmenite and leucoxene for Ti. Refining processes such as the Van Arkel de Boer and Kroll-reduced processes are used to produce 99.99% pure titanium sponge and 99.94% electrolytic nickel required for ingot-casting of NiTi alloys [13, 31].

NiTi casting methods include Vacuum Induction Melting (VIM), Vacuum Arc Remelting (VAR)

and Electron Beam Melting (EBM). In VIM, high purity Ni and Ti (as quantified above) are placed in a graphite crucible for simultaneous melting under vacuum or inert gas atmosphere. Eddy currents produced by induction coil are used to melt Ni and Ti simultaneously at temperatures between 1510 K and 1723 K. VAR utilizes a consumable or non-consumable electrode consisting of pure Ni and Ti and heats it using argon arc to form a button-shaped or cylindrical ingot. EBM casting method uses electron beam to melt Ni and Ti in a water-cooled copper crucible under high vacuum conditions. Due to high operating conditions, it is difficult to control nominal composition of NiTi and thus martensitic transformation temperatures are affected [13].

An alternate means of manufacturing NiTi from pure Ni and Ti is powder metallurgy. Pre-alloyed or elemental powders of Ni and Ti are combined together by blending, pressing and sintering. Compared to the casting methods, powder metallurgy provides better control over transformation temperatures as it does not involve a melting process which causes composition inaccuracy [13].

2.2.2 Hot Working

As-cast microstructure and surface properties of NiTi are not acceptable for medical and automotive applications, and post-processing techniques such as hot-working and cold-working are required. Hot working procedures include press forging, hot rolling and rotary forging [13].

In hot working, NiTi is heated in the range of 300-900 °C, with significant softening occurring near 400 °C and 100% elongation occurring near 900 °C due to a reduction in critical flow stress as temperature increases [32-34]. Generally, cracks appear at 900 °C due to oxide embrittlement, and therefore, for good workability and reduced oxidation, 800 °C is preferable [35]. However, oxidation can still occur at 800 °C, hence, copper, mild steel sleeve canning or extrusion methods are used to minimize oxidation [36-38]. Between 400-600 °C, dynamic recrystallization and precipitation formation occurs, but long range recrystallization does not occur and elongated grains are typical of the microstructure [39, 40].

2.2.3 Cold Working

Cold working of hot-worked NiTi is normally performed to provide final product shape, fine microstructure and desired mechanical properties for different applications [30]. Relative to hot-

working, cold-working leads to much greater retained martensite and amorphization [41]. Also, cold working below M_f (marforming) results in finer subgrains than above M_d (ausforming), because dislocation annihilation and dynamic recrystallization do not occur at lower temperature [37]. Ausformed parts are more thermally stable and less sensitive to heat treatment [37], whereas marformed parts provide higher strength, stability and fatigue life [42]. Typically, 30-40% cold working is the acceptable range for cold-working as NiTi work hardens quickly. To perform further cold-working, full annealing at 600-800 °C is required [30].

2.2.4 Heat Treatments

Cold-worked NiTi needs to go through heat treatment to restore SMA properties, provide precipitation strengthening for Ni-rich NiTi and increase resistance to fatigue crack nucleation [43]. The formation of Ni-rich precipitates through post-processed heat treatment is used to alter functional properties of NiTi SMA, as mentioned in **section 2.1.5: Physical Metallurgy and NiTi Composition**. The inclusion of these precipitates in the NiTi matrix leads to increased transformation temperatures which results in decreased σ_{SIM} due to reduction in the stability of austenite [20]. **Figure 2-10** shows a time-temperature-transformation graph illustrating the relationship between heat treatment time and temperature.

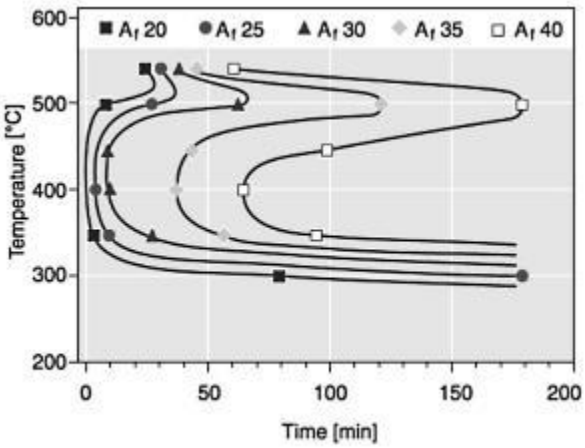

Figure 2-10: Time-temperature-transformation (TTT) diagram showing relationship between heat treatment temperature, time and A_f temperatures [24]

To obtain a good microstructure, percent cold work, heating temperature and time need to be controlled appropriately [24, 30]. Intermediate temperatures between 350 and 475 °C results in optimization of nucleation and diffusion for maximum, coherent, fine precipitate formation [24,

44]. Typically, based on various sources, heat treatment at 400 °C for about an hour provides the most stable properties for both Ni-rich and Ti-rich NiTi [13, 26, 44, 45]. After heat treatment, NiTi must be quenched to avoid the formation of Ni_3Ti [46].

2.3 Laser Processing Fundamentals

Generally, laser welding has been the primary laser processing technique used to process NiTi SMAs. High sensitivity of functional properties to thermal events, low heat input and high cooling rate have given laser welding the edge as far as laser processing is concerned [47]. Vaporization of alloying components during keyhole welding by a high energy density source, such as a laser, is a well-documented trait which has exemplified importance in the loss of chromium during laser welding of stainless steel [48-50]. In NiTi, Ni has higher vapor pressure compared to Ti, and therefore, NiTi experiences preferential vaporization during keyhole laser welding [6]. However, this vaporization is limited to the initial creation of keyhole, after which, the effect of vaporization on material composition is negligible [50]. Therefore, continuous laser welding would have minimal effect on NiTi composition, and may also introduce unwanted oxides in the weld [51].

Pulsed laser processing, on the other hand can significantly change the composition and thus the transformation temperature of the material as observed in **section 2.1.5: Physical Metallurgy and NiTi Composition**. The ability to locally modify composition, and achieve high precision and quality makes pulsed laser processing an excellent technique for processing SMAs [6, 52]. Also, it allows for the creation of monolithic components with varying functional properties.

2.3.1 Laser System

A laser system consists of three main components namely amplifying medium, pump source and an optical resonator [53]. The amplifying medium consists of a special material that produces energy-carrying photons when excited. The pump source, which is a means to stimulate the medium to its amplified state, is determined by the type of active medium used. The optical resonator is composed of two parallel mirrors which are completely and partially reflective. They are positioned around the active medium to filter and transmit photons that fulfill the specific requirements for oscillation [53].

Pumping leads to the excitement of atoms from ground state to excited state when the laser system

is activated. Incoherent photons are then released when the atoms relax back to ground state. Some photons are lost in the resonator due to their non-parallel route relative to the optical axis, while others travelling parallel to the optical axis are oscillated in the resonator with possibility of inducing stimulated emission, which leads to the production of coherent photons [53]. A high energy laser beam is created by increasing the number of unidirectional photons.

Population inversion is defined as the phenomenon where the number of photons being amplified exceeds the number being absorbed. This is required to amplify the quantity of incident light [54]. When population inversion occurs in the cavity, the excited atoms and laser interact to lower the energy level and reduce additional quanta of light [55]. The energy of the laser beam is reduced if this does not occur, as otherwise, energy absorbed from the laser is used to excite the atoms. Finally, the amplified laser beam is released through a partially reflective mirror in the cavity as shown in **Figure 2-11**.

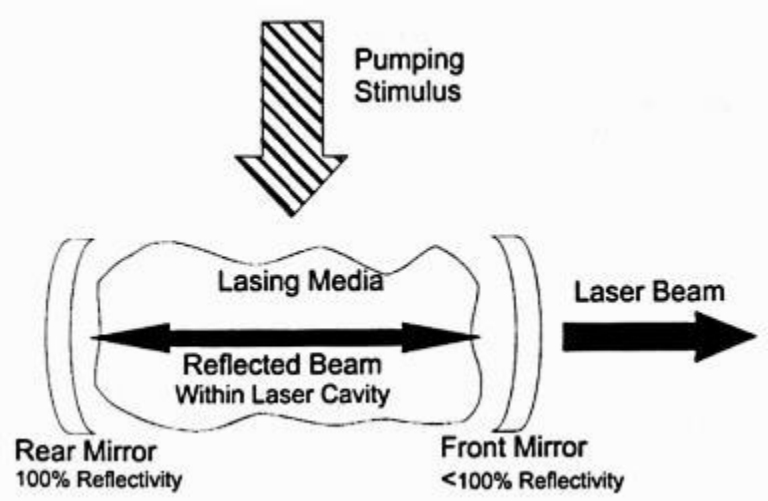

Figure 2-11: Diagram showing the production of a laser beam [56].

2.3.2 Pulsed Nd:YAG Laser Processing

Different lasers generate light with unique wavelengths, which depend on the material used to make the semiconductor. Wavelengths range from 0.1 µm to 10 µm, with Nd:YAG producing one of the shorter wavelengths available. Nd:YAG is more efficient compared to other lasers as the energy emitted by the Nd:YAG laser can be more efficiently absorbed by most materials leading to efficient melting of a specific volume of material. Commercial Nd:YAG lasers are rated with average output powers from 0.3 kW to 3 kW, which is ideal for small scale use [53].

Figure 2-12 shows a schematic of a Nd:YAG laser system. The cavity assembly includes an active medium, pumping source and resonator. When excited, an yttrium aluminium garnet (YAG) crystal doped with neodymium (Nd) atoms produces photons with a wavelength of 1064 nm [53]. A flash lamp acts as the pump source of the Nd:YAG laser [53]. The laser output is transmitted through input coupling optics and into an optical fiber connected to the working head before being directed to the workpiece. Photon delivery via fiber optics is advantageous for fabrication of complex components.

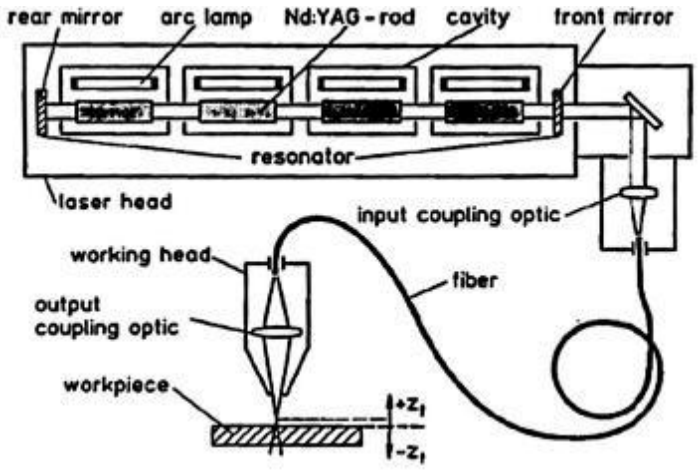

Figure 2-12: Schematic of Nd:YAG laser setup [27].

2.3.3 Processing Parameters

Laser processing parameters play a crucial role in controlling vaporization of Ni in NiTi. Some key parameters include pulse width, peak power, frequency, travel speed and defocus distance. A schematic of a temporal profile of laser pulses produced by Nd:YAG laser processing is shown in **Figure 2-13**. Peak power is defined as the maximum power of the laser pulse. Pulse width is the duration of the pulse, which typically varies from 0.2 to 20 ms. Pulse energy is calculated based on the area under each laser pulse. The average power delivered to the workpiece is derived from the pulse energy and frequency. However, determining the exact quantity of energy absorbed by the workpiece is challenging due to the possibility of reflection, which could result in significant energy losses.

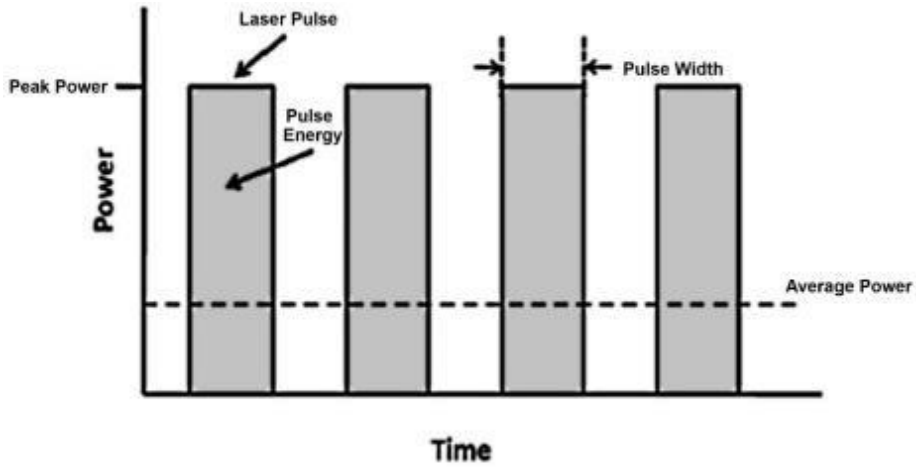

Figure 2-13: Graph of Nd:YAG pulse power versus time [27].

One major advantage of laser processing is the ability to produce high energy densities, which could maximize penetration of the workpiece. To achieve this, the light needs to be focused to a minimum beam waist diameter, or the spot size needs to be focused at zero defocus distance [53] as shown in **Figure 2-14**. Offsetting defocus distance results in reduction of laser power density. Focus spot size depends on the combined effects of optics, laser characteristics and welding parameters. The focus position relative to the workpiece depends on the mode of laser beam operation (discussed in **section 2.3.5: Laser Beam Modes**) and geometry [53]. Generally, best practice is to focus at a distance where the penetration depth is maximized through experimental verification. Highest energy efficiency is attained when the laser operates in its convergence range.

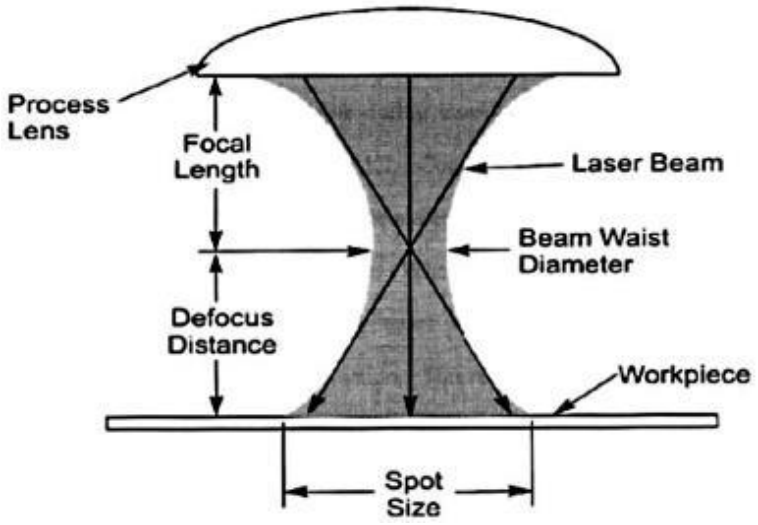

Figure 2-14: Diagram showing propagation and convergence of a laser beam [56].

2.3.4 Shielding Gas

To avoid reaction of oxygen or nitrogen with the molten weld pool during laser processing of metal, a shielding gas such as argon or helium is generally used. Oxide inclusions typically deteriorate material properties [53, 57]. For NiTi SMAs, shielding is critical due to its high affinity for oxygen, and, to lesser extent, nitrogen. Careful selection of shielding gas increases the possibility of enhanced transmission of the incident laser beam for absorption by the workpiece [54].

2.3.5 Laser Beam Modes

There are two main laser beam modes, namely, conduction and keyhole as shown in **Figure 2-15**. During conduction mode, the laser intensity is only sufficient to melt the workpiece. The pool forms at the surface and grows in all directions, which results in a semi-elliptical shape as shown in **Figure 2-15 (a)** [27].

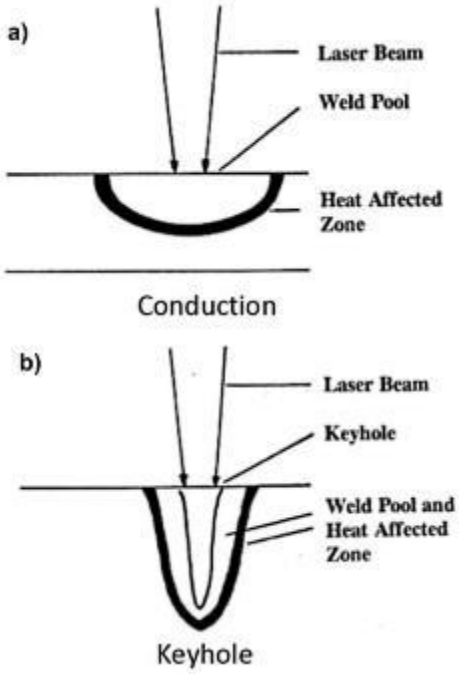

Figure 2-15: Comparison of (a) conduction and (b) keyhole laser beam modes [57].

Due to the absorption of laser energy at the surface of the material, surface reflection will likely occur, leading to reduced absorption by the workpiece. Alternatively, keyhole mode occurs when the peak temperature at the surface is high enough to vaporize the workpiece material. Pressure of

vaporization leads to the formation of a conical-shaped weld pool and heat-affected zone (HAZ) as shown in **Figure 2-15 (b)** [27]. Since the laser energy is trapped within the keyhole and there is minimal surface reflectivity, the laser energy is transmitted more efficiently compared to conduction mode.

2.4 Wire Drawing Basics

Wire drawing is performed to reduce the diameter of the as-received wire as per application requirement. Normally, the maximum reduction per pass is limited to 30-35% and much lower amounts of reductions are used for non-ferrous materials [58]. Circumferential reduction of the wire occurs as it passes through the die due to a complex interaction between the wire and the walls of the die [59].

The reduction of cross sectional area can be calculated as shown in equation (**Equation (2-2)**):

$$R = 1 - \frac{A_1}{A_0} \tag{2-2}$$

The symbol R represents the reduction in wire cross-sectional area after wire-drawing, A_0 is the initial cross-sectional area of the wire before wire-drawing and A_1 is the final cross-sectional area. This reduction, in conjunction with die angle α, can be used to determine the area of idealized deformation, as shown in the trapezoidal section in **Figure 2-16** below. The wire drawing reduction and the die angle can be characterized by the relationship between R and α, Δ, which has a large effect on wire drawing deformation, as shown in **Figure 2-17**. Ideally, Δ should be close to 1 for uniform wire-drawing [58].

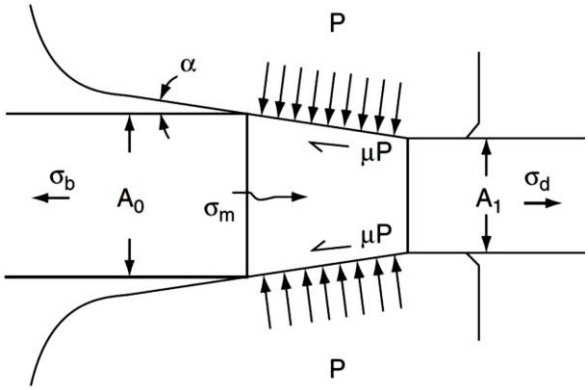

Figure 2-16: An analytical schematic of drawing through a die [58].

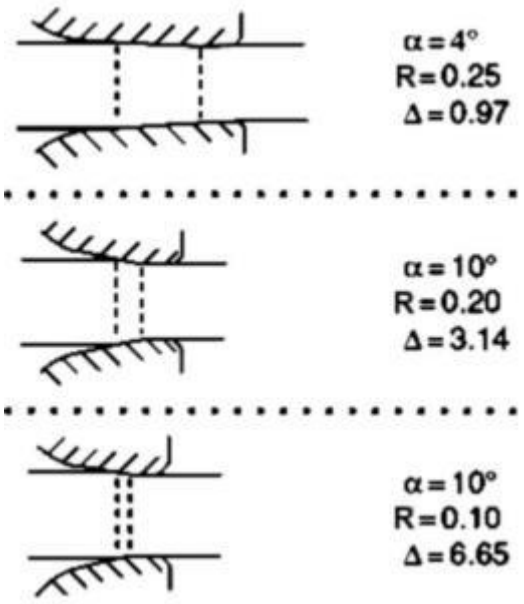

Figure 2-17: Wire drawing examples for three different deformation zones [58].

Increased values of Δ (around 2-3) can be attributed to engineering constraints such as drawing stress which needs to be less than 0.6 times the existing wire's yield stress [59]. Drawing stress is defined as the sum of uniform work (W_U), redundant work (W_R) and frictional work (W_F). Uniform work thins and stretches the wire, while redundant and frictional work assist in wire reduction [58]. The redundant work is related to change in direction of material flow at die entrance and exit, and it increases significantly as Δ increases due to non-uniform strain [60]. On the other hand, frictional work is defined as the work done at the interface of the wire and the die, and results in increased wire temperatures, which must be cooled to avoid recrystallization, lubricant deterioration, or die-sticking [61].

To obtain lower values of Δ, reduce die wear, frequency of intermediate annealing steps and risk of breaking wire, adequate lubrication is required [62, 63]. Lubrication also improves ductility and reduces the potential for drawing stress higher than wire flow stress [64]. Wire drawing consistency can be achieved by ensuring Δ values are similar for consecutive wire drawing stages, and die is aligned concentric with the wire so that the forces are evenly distributed across the die cone for even deformation [59].

2.4.1 Wire Drawing SMAs

NiTi SMAs usually require thin oxide lubricant such as MoS_2 to promote lower drawing stresses,

increased drawing stability and improved wire-drawn quality [65]. Heating of the NiTi wire due to increased frictional work results in the transformation from the preferred marforming to the undesired ausforming [61]. When no lube is used, the wire surface has heavy striations and string bonds form between the wire and the die, which results in a fracture surface and metal stuck in the die [66]. Furthermore, non-continuous lubrication results in local effects termed 'crows feet' which occur due to shear fracture. This leads to reduced lubricant efficacy resulting in die wear, reduction of physical and fatigue properties, and the potential for breaking the wire, which can jeopardize the final outcome of the wire-drawing process [66].

Final cold-work percentages between 20-50% have been determined to provide good physical properties, transformation stability and fatigue life [13, 24, 67-69]. A comprehensive examination of NiTi wire manufacturing has been performed by Grossman et al., but even this publication does not highlight the final cold-working steps [70]. For wire-drawing NiTi, it is crucial to know the number of passes between equivalent reductions to maintain uniformity of hardness across the cross-section as shown in **Figure 2-18**. Multiple passes around the M_s result in lowest critical stress for deformation, which leads to lower drawing stress and increased number of passes between annealing stages, as shown in **Figure 2-19**. Drawing in R-phase results in even lower stress due to its low critical stress for deformation [71]. The final texture of NiTi after wire-drawing is in the <111> direction, which leads to the largest recoverable strain [72].

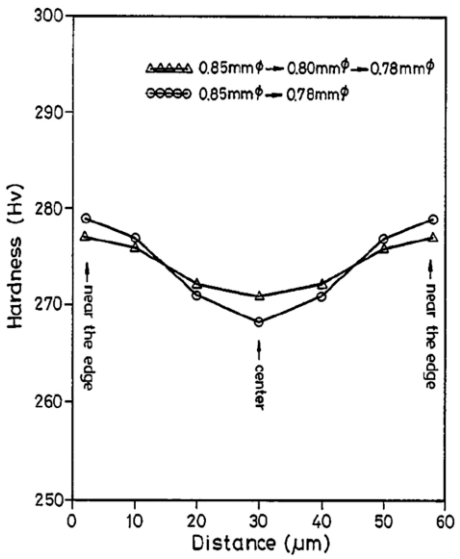

Figure 2-18: Hardness curves on a NiTi wire cross-section drawn from 0.85 mm diameter to 0.75 mm diameter [70].

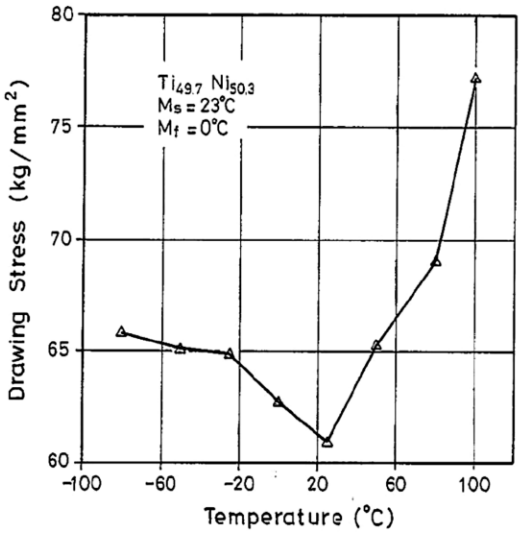

Figure 2-19: Drawing stress versus temperature for NiTi wire [70].

2.5 Spring Actuator Design

The second major topic required to understand NiTi self-biasing spring actuators is spring design. Springs are objects which store potential energy by straining the bonds between the atoms of an elastic material [73]. Springs are generally made out of hardened carbon steel, however, as of recently, NiTi springs are being used in cars and aeroplanes for various applications.

The actions of a spring (such as compression and extension) are governed by Hooke's law, which states that the force (F) required to deform a spring is proportional to the spring's displacement (x) by a constant factor (k), as shown in **Equation (2-3)** below:

$$F = k * \mathrm{x} \tag{2-3}$$

The constant factor k is also known as stiffness, spring rate or spring constant and has a SI unit of N/m. It is defined as the slope of the force deflection curve of the spring, where deflection or displacement is sometimes denoted with the symbol δ, and is measured in metres (m). Applied or deforming force is measured in Newtons (N).

Types of springs include tension, compression, leaf, spiral, Belleville (or washer), torsion (such as helical or coil), cantilever and gas springs. The most common types of springs are tension and compression springs due to their relative simplicity and ease of manufacturing compared to other springs. In this thesis, major emphasis will be placed on compression springs because they are the

most familiar spring types available [74].

2.5.1 Helical Compression Springs

Some of the most common types of springs available in the market are helical compression springs. Typically, they are manufactured with a constant pitch (p) and wire diameter (d) as shown in **Figure 2-20**. Before manufacturing compression springs though, a number of spring constraints, such as spring index, spring shear stress, spring load, pitch, number of active coils, and wire diameter need to be considered to avoid spring failure during loading. The mean spring diameter (D), wire diameter (d), free length (L_f), and either number of active coils (N_a) or pitch (p) are generally used in spring design to determine spring geometry and perform associated analysis.

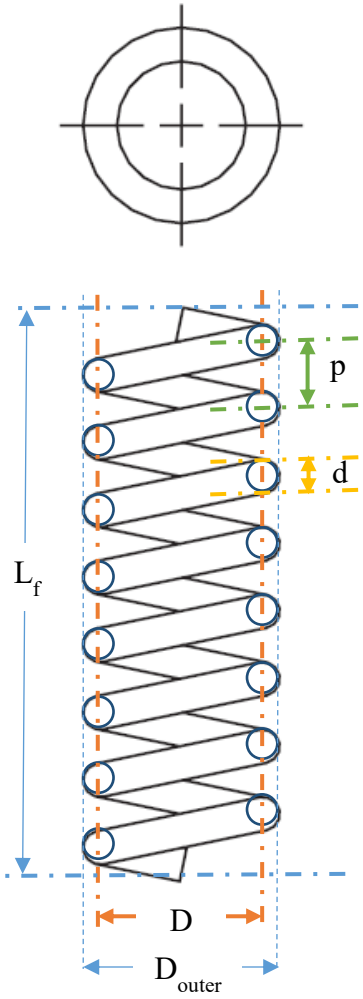

Figure 2-20: Helical Compression Spring Design Parameters.

2.5.1.1 Spring Index

Spring index (C) is defined as the ratio of the mean spring diameter (D) to the wire diameter (d) as shown in **Equation (2-4)** below:

$$C = \frac{D}{d} \tag{2-4}$$

Preferred spring index values for helical compression springs lie between 4 and 12 with an optimum value of approximately 9. For values below 4, springs are difficult to manufacture due to tooling stresses. For values above 12, springs have an increased likelihood of buckling [74]. However, springs with spring index values between 4 and 5 are hard and costly to manufacture. Therefore, an acceptable range for manufacturing springs is generally between 6 and 12. Smaller spring index results in larger applied force, and therefore stronger spring, as shown in **Equation (2-5)** below, where G is the shear modulus of elasticity of the material.

$$F = \frac{Gd\delta}{8C^3N_a} \tag{2-5}$$

2.5.1.2 Spring Rate

Spring rate is defined as the change in load (force) per unit deflection, as derived from **Equation (2-3)** above and is measured in N/m. However, a relationship between spring constant and number of active coils can also be obtained from **Equation (2-5)** by replacing F with kδ, as shown in **Equation (2-6)** below.

$$k = \frac{Gd}{8C^3N_a} \tag{2-6}$$

As the number of coils or spring index increases, the spring constant decreases. On the contrary, shear modulus is directly proportional to spring constant. Therefore, to achieve high spring rates, a material with large shear modulus, low spring index and/or smaller number of coils can be chosen for spring fabrication.

2.5.1.3 Natural Frequency

When springs are excited near their natural frequency, they tend to vibrate both laterally and longitudinally. So, if a helical spring, fixed at one end, is given a sufficient rapid compression at the other end, the end coil will be pushed against its neighbour before the remaining coils respond to the displacement [74]. This process is carried over one coil at a time until the compression wave reaches the coil at the fixed end, where the disturbance is finally reflected back. The motion is eventually damped out after several repetitions of compression wave propagation. This behaviour is classified as spring surge and causes very high stresses in the spring (identical to those obtained when spring is compressed to its solid height). The spring surge relies on boundary conditions. For the fixed-fixed case in equation **Equation (2-7)**,

$$f_n = \frac{1}{2}\sqrt{\left(\frac{k}{m}\right)} \tag{2-7}$$

where f_n is the natural frequency, in Hz, and m is the mass of the spring, in kg.

Substituting in the mass of a helical compression spring in **Equation (2-7)**, **Equation (2-8)** is derived:

$$f_n = \frac{d}{2\pi D^2 N}\sqrt{\left(\frac{G}{2\rho}\right)} \tag{2-8}$$

The symbol ρ denotes the density of the spring wire, and N is the total number of coils in the spring. To avoid spring surge during cyclic loading, the natural frequency should be at least 13 times the forcing frequency of the load. The higher the natural frequency, the higher the maximum stresses as mass is reduced [74].

2.5.1.4 Ultimate Tensile Strength

Values for ultimate tensile strength of a spring wire is found to vary with wire diameter, and are shown in **Figure 2-21** for different materials. The ultimate tensile strength is indirectly proportional to the wire diameter which implies that increase in spring wire diameter leads to decrease in minimum ultimate tensile strength. Since reduction of wire diameter requires wire-drawing, the smaller the wire diameter, the more cold-worked the material. This leads to increased dislocations which results in increased UTS due to decreased dislocation motion.

2.5.1.5 Critical Buckling

In addition to keeping the spring index value below 12, a couple of other factors need to be considered to avoid buckling of a spring. Buckling may occur if springs are too long ($L_f > 4D$). The ratio of free length to the mean coil diameter (also known as the slenderness factor), the ratio of deflection to free length and types of ends determine if buckling will occur or not [74]. Critical buckling occurs with values to the right of curves A and B in **Figure 2-22**. Curve A depicts the buckling regime for a compression spring with one end fixed and the other end free to tip. On the other hand, curve B has one end fixed and the other end fixed against tipping as shown in **Figure 2-23**.Buckling occurrence is lower in springs retained between two parallel plates as shown in **Figure 2-23** and indicated in **Figure 2-22**, where the area of stability is larger for curve B.

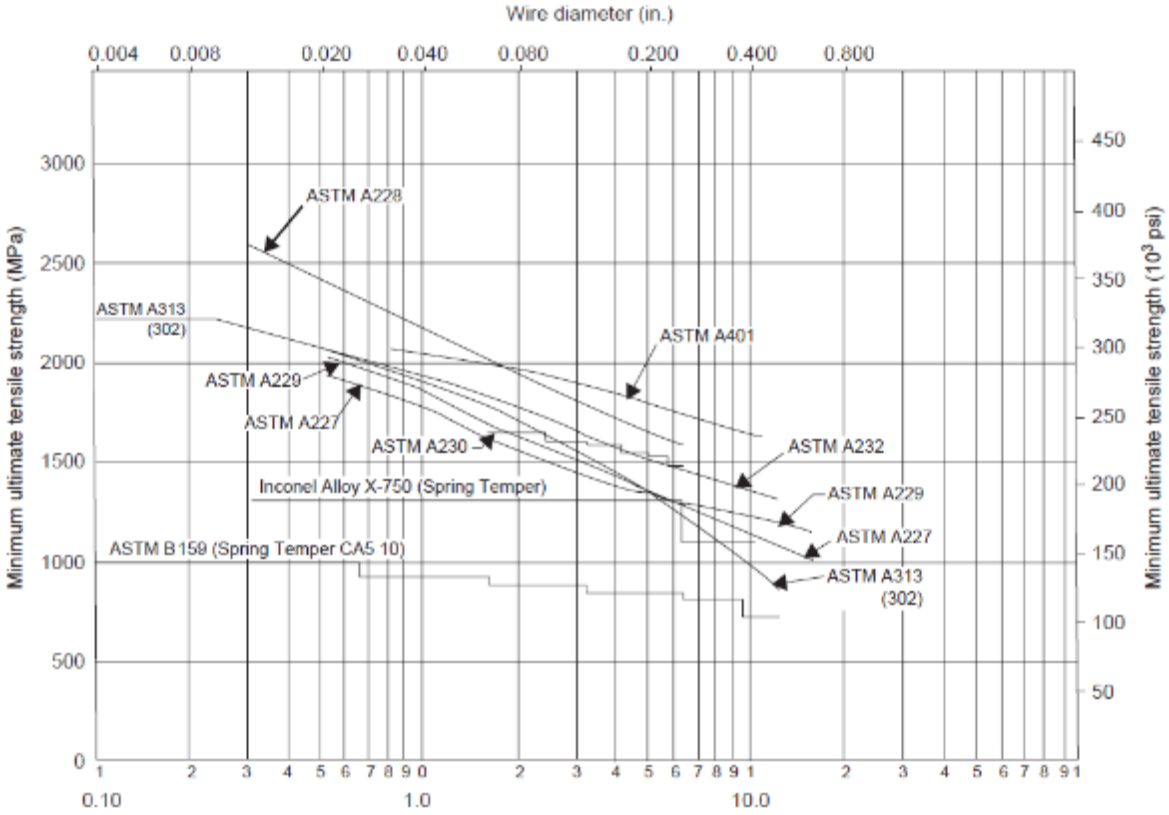

Figure 2-21: Minimum ultimate tensile strengths versus wire diameter for different spring material [75].

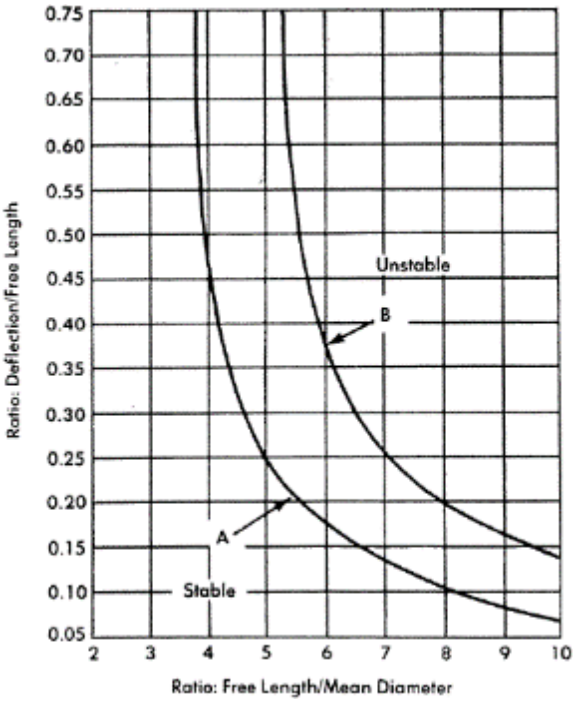

Figure 2-22: Critical Buckling Curves.

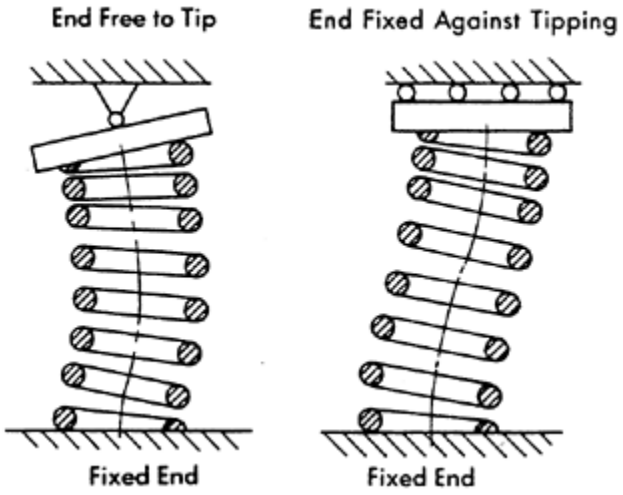

Figure 2-23: End conditions used to determine critical buckling [75].

2.5.1.6 Shear Stress and Wahl's Correction Factor

There are two main components of stress acting on a helical compression spring during loading. The principle stress that maxes out at the surface of the wire (inner diameter of spring) is the torsional shear stress. Accompanying this stress is the less significant direct shear stress, which can be approximated by dividing the applied force (F) by the cross-sectional area (A) of the wire.

These two stress components are illustrated in **Figure 2-24**.

To avoid failure of compression spring during dynamic or static loading, the maximum shear stress at the inner diameter of the helical compression spring must be calculated by summing up the two stress components described above. **Equation (2-9)** shows this stress:

$$\tau_{max} = K_s \frac{8FD}{\pi d^3} \tag{2-9}$$

where K_s is the direct shear stress factor which does not include stress due to curvature of spring. **Equation (2-10)** shows the actual definition of K_s:

$$K_s = 1 + \frac{1}{2C} \tag{2-10}$$

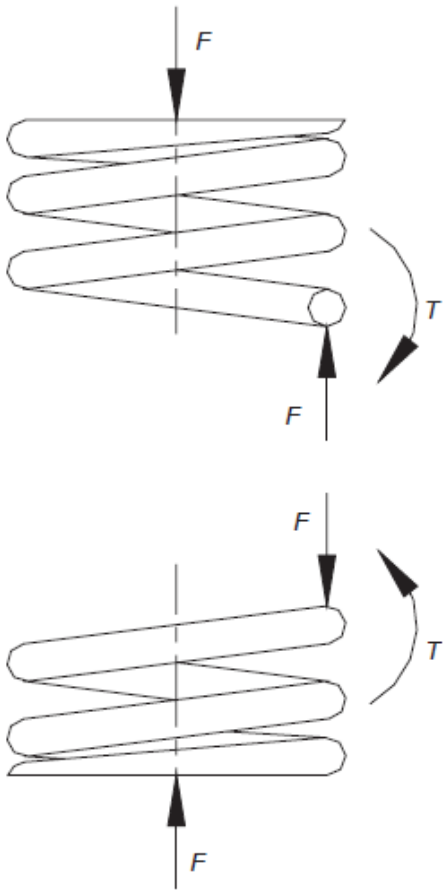

Figure 2-24: Free body diagram of a helical compression spring loaded with force F.

In 1944, A.M. Wahl determined a new correction factor, termed Wahl's correction factor (K_w), which incorporates the stress due to spring curvature in addition to the direct and torsional shear stresses. **Equation (2-11)** describes the relationship between K_w at the inner diameter of the spring and the spring index:

$$K_w = \frac{4C - 1}{4C - 4} + \frac{0.615}{C} \tag{2-11}$$

At the outer diameter of the spring, the correction factor is defined by **Equation (2-12)**:

$$K_w = \frac{4C + 1}{4C + 4} + \frac{0.615}{C} \tag{2-12}$$

Since the correction factor in **Equation (2-12)** is smaller than that in **Equation (2-11)**, it can be concluded that the maximum stress occurs at the inner diameter of the spring.

Replacing K_s (**Equation (2-10)**) with K_w (**Equation (2-11)**) in **Equation (2-9)** above yields the maximum shear stress beyond which the spring fails during loading.

$$\tau_{max} = K_w \frac{8FD}{\pi d^3} \tag{2-13}$$

Therefore, **Equation (2-13)** above indicates the maximum stress at the inner diameter of the wire, where the point of fracture initiation is located [76]. **Figure 2-25** below shows the relationship between Wahl's factor and spring index. To obtain a spring with an acceptable spring index, Wahl's correction factor (K_{w1}) needs to lie between 1.12 and 1.25 approximately. Generally, K_{w2} (identical to K_s) is used in conditions (such as elevated temperatures) when resultant stresses are distributed more evenly around the cross section of the spring wire (after spring set is removed) [77].

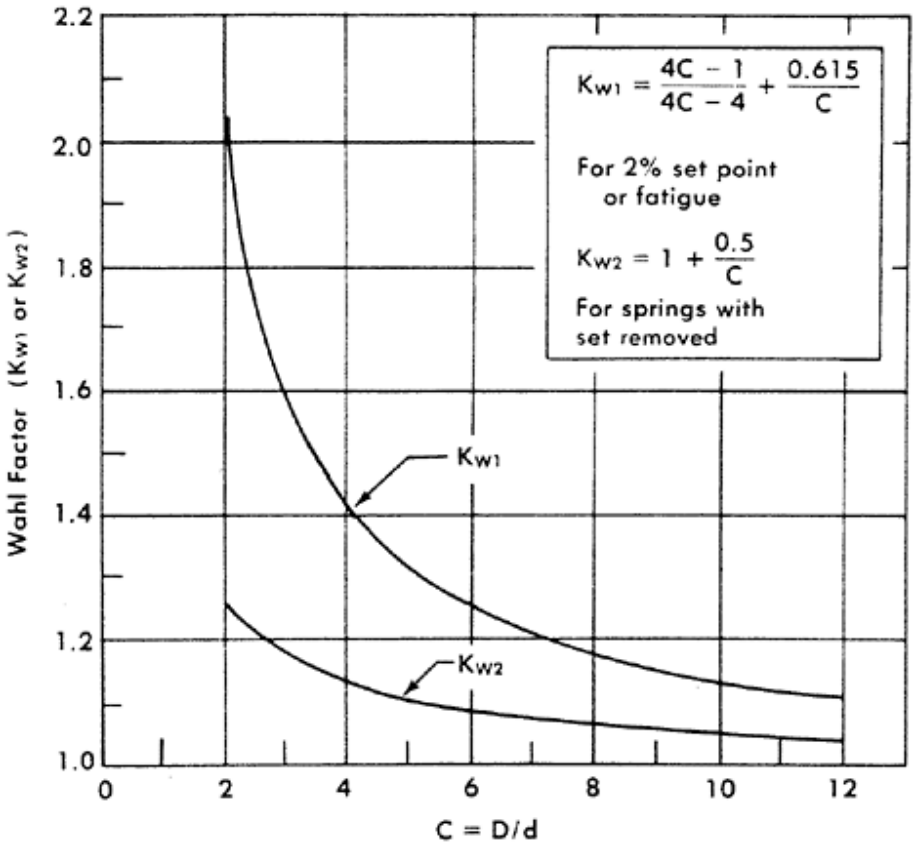

Figure 2-25: Wahl's factor versus spring index [75].

However, the maximum stress obtained from **Equation (2-13)** holds only as long as the elastic conditions prevail, i.e., as long as the yield point is not exceeded. Beyond the elastic limit, the actual maximum stress could be lower than the derived value. Also, it is unlikely that a load will directly be on a spring's geometric axis. Eccentric loading of a compression spring causes stresses on one side of the spring to be higher than indicated in **Equation (2-9)** and **Equation (2-12)** [74].

2.5.1.7 Types of spring ends

Compression springs can be manufactured to have one of the following types of ends: (1) plain end; (2) plain end ground; (3) squared end; (4) squared and ground end. **Table 2-2** lists equations for number of active coils (i/N_a), total number of coils (i^t/N_t), free length (l_f), pitch (p) and solid height (h) for different spring ends.

Table 2-2: Equations for helical compression springs with different types of ends [78].

	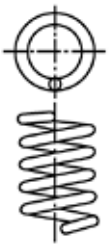 (a) Plain	 (b) Ground	 (c) Squared	 (d) Squared and ground
Particular				
Active coils, i	i'	$i' - \frac{1}{2}$	$i' - 2$	$i' - 2$
Total coils, i'	$\frac{l_o - d}{p}$	$\frac{l_o}{p}$	$\frac{l_o - 3d}{p}$	$\frac{l_o - 2d}{p} + 2$
Free length, l_o or l_f	$ip + d$	ip	$ip + 3d$	$ip + 2d$
Pitch, p	$\frac{l_o - d}{i'}$	$\frac{l_o}{i'}$	$\frac{l_o - 3d}{i'}$	$\frac{l_o - 2d}{i'}$
Solid height, h	$d(i' + 1)$	$d(i' + \frac{1}{2})$	$d(i' + 1)$	$i'd$

2.5.1.8 Manufacturing

Industrial spring manufacturing occurs with huge automated robotic arms which allow quick and efficient production of springs in bulk. Wire springs, which include compression, tension and torsion springs among others, are generally manufactured by wrapping a piece of wire up to 0.75 in (18 mm) in diameter, made out of processed (typically cold-rolled) carbon steel with approximately 0.5 to 1.2% carbon content [handbook of mechanical spring design] [79], around a metal shaft (also known as an arbor or mandrel) and heating the spring at relatively high temperatures to stabilize and strengthen the shape of the spring, and remove residual stresses.

For large-scale spring production in industries, hot-winding is typically used if wire diameter is 3 in (75 mm) at most. The steel is coiled around a mandrel while red hot, quenched down to martensitic temperature, and tempered to strengthen and remove residual stresses in the spring. After heat-treatment, the wire is ground down to improve the bearing surface. Ground and squared ends generally tend to have bearing surface of 270 to 330° to reduce the chance of buckling.

2.5.2 SMA Compression Spring

Compared to conventional steel springs, helical SMA compression springs are more suitable for spring actuators because they are lighter and produce larger forces. At lower weights, SMA spring

actuators have the highest power/weight ratio compared to other conventional actuators (see **Figure 2-26**) which makes them ideal for light-weight automotive applications [5].

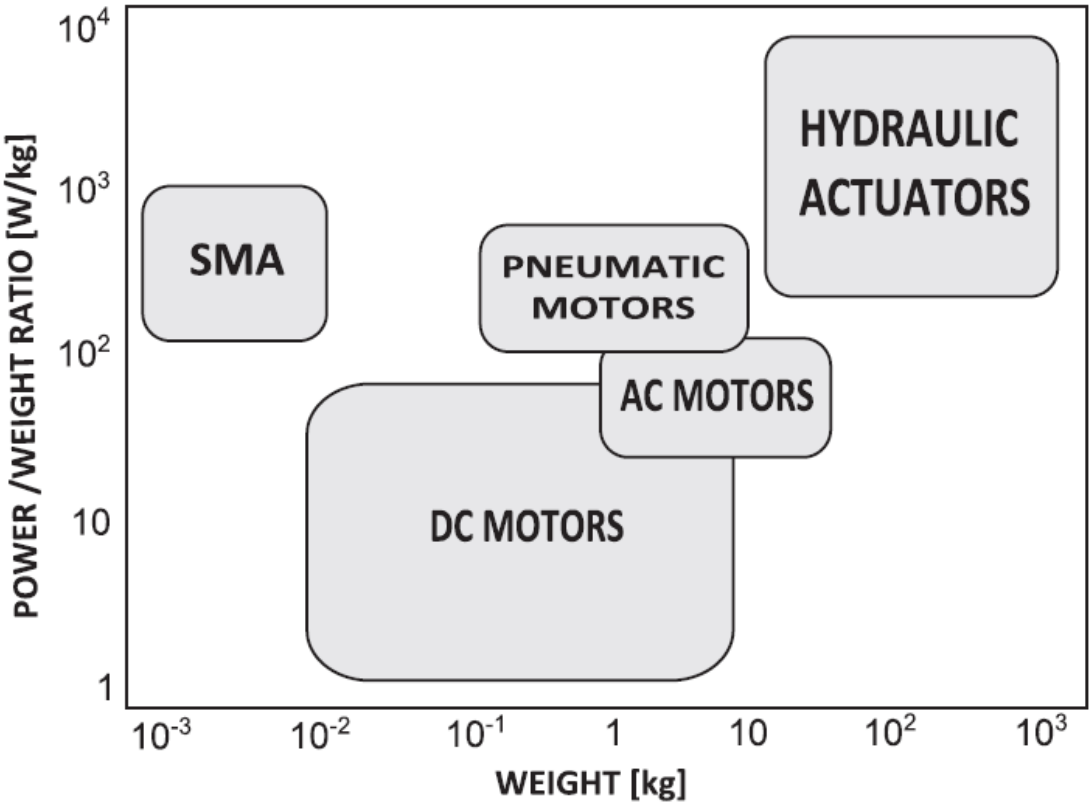

Figure 2-26: Power/weight ratio versus weight of common actuation [5].

SMA spring actuators can be subdivided into two different categories namely thermal actuators and electrical actuators. Thermal actuators combine the sensing and actuating functions, responding to temperature change by changing shape and/or generating a force [3]. Electrical actuators respond to electrical signal and move an object or perform a task on demand. Typically, a current is passed through the electrical SMA actuator to heat it above A_f for shape recovery [3].

2.5.2.1 Thermal Actuators

SMA thermal actuators are used in a variety of automotive applications summarized in **Figure 2-27**. Three different temperature ranges are known to be beneficial for applications in cars. Temperatures below 0 °C are suitable for low temperature performance in engine, transmission, suspension and brakes; temperatures between 0-60 °C are favourable for cold start performance

and climate control; and, temperatures between 60-120 °C are used for cooling system, restart ability, climate control and rattling [3].

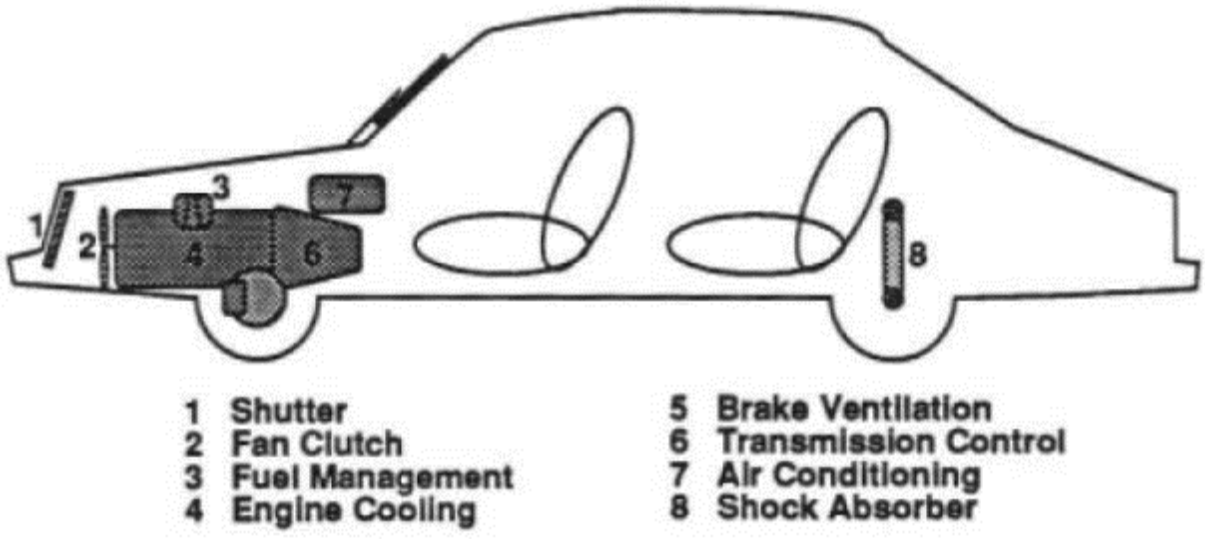

Figure 2-27: Potential applications of thermal actuators in [3]

Generally, transformation temperatures from -20 °C to approximately +80 °C are suitable for multiple cycle operations due to large hysteresis width (30 to 50 °C) and better stability during cycling. Binary NiTi alloys with temperatures above 80 °C are convenient for single cycle applications [3].

2.5.2.2 Thermomechanical Behaviour

To better understand the significance of SMA spring design for use in spring actuators, the thermomechanical behaviour needs to be studied. Analysis of thermomechanical behaviour involves studying the effect of temperature on the mechanical properties of SMA springs. Constitutive, experimental and conventional spring design models have previously been used to depict the thermomechanical behaviour of SMA springs [80-83]. Constitutive thermomechanical models are complex and difficult to use directly as design models without direct knowledge of numerical and computational methods [84]. Models based on experimental characterization or conventional spring design are simpler to use [84]. Experimental characterization involves heating SMA spring actuators in a thermal chamber or using electrical current, and studying the mechanical response at different temperatures, whereas, conventional spring design uses the linear

coil spring equation to study the spring's mechanical response at different temperatures. Typically, for both experimental and conventional techniques, force-deflection plots of SMA springs in fully martensitic ($T<M_f$) and fully austenitic ($T>A_f$) states are sufficient to determine the maximum force and deflection of the spring actuator [84].

Force-deflection plots of actuation behaviour for SMA springs are shown in **Figure 2-28**. Figure 2-28 (a) shows non-linear behaviour of an actual SMA coil spring actuator while Figure 2-28 (b) shows linear behaviour of a conventional spring design formula. Comparing force-deflection plots for both models reflects the inaccurate prediction of the martensitic mechanical response for the conventional spring design. This occurs because the conventional design does not account for the elongation of the coil spring actuator due to detwinning, which is a significant mechanism for SME [84]. Therefore, experimental characterization of a SMA spring actuator provides a more accurate model of its thermomechanical behaviour.

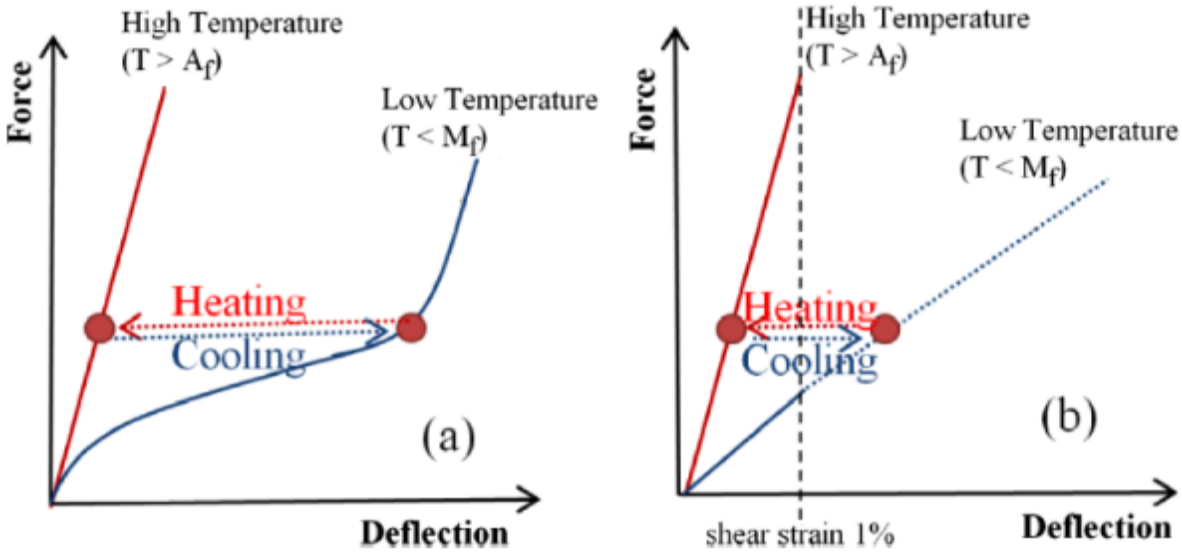

Figure 2-28: Force deflection curve for (a) actuation behaviour and (b) curve based on conventional spring design [84].

2.5.2.3 Spring Stroke

Similar to conventional spring design, SMA compression spring design also requires the use of parameters such as pitch, wire diameter, spring diameter and number of active coils to optimize spring properties for temperature-sensitive actuation. However, the maximum stroke is the most important design constraint for SMA spring actuator design.

Design parameters necessary for determining stroke are shown in **Figure 2-29**. k_A^* is the slope of the austenite curve, F_p is the force level at the end of the plateau and ε_{net} is the difference in strain between the end of the martensite plateau and the point on the austenite curve at the same force level [85].

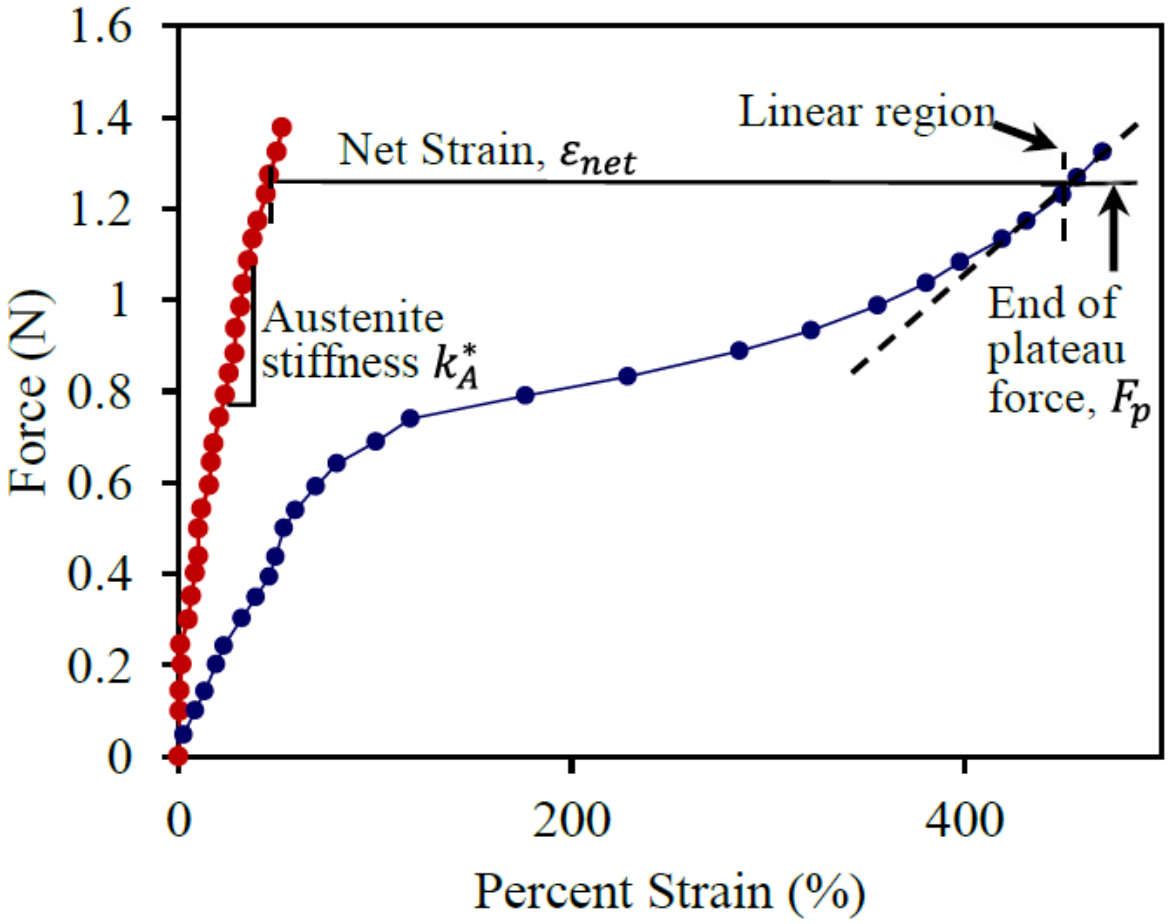

Figure 2-29: Force-strain curve indicating design parameters for stroke measurement of SMA helical spring [85].

Stroke produced by the actuator at the end of the martensite plateau is:

$$\delta = \varepsilon_{net} L_0, \tag{2-14}$$

where L_0 is the austenite free reference length of the actuator [85]. The larger the stroke is, the larger the actuation that is achievable in the helical coil actuator.

2.5.2.4 Manufacturing

Unlike steel springs, SMA spring manufacturing is typically done manually because of the requirement to shape-set the SMA wire to a spring shape. The SMA spring wire must be processed, cold-worked to the desired wire diameter, and softened by heat before shape-setting. Various methods have previously been used to make helical SMA springs [5, 85]. Typically, SMA wires are fixed on one end to a spring mandrel and coiled around a rod using a mechanical tool (e.g. crank), while the other end is attached to a weight. After coiling, the other end is fixed to the spring mandrel to hold its shape, and shoved into a pre-heated oven at a temperature between 350-475 °C. After heat treatment, the mandrel is quenched in cold water to avoid the formation of brittle Ni-rich precipitates (see **section 2.2.4: Heat Treatments**). One major drawback in this method is that spring pitch cannot be accurately controlled.

Chapter 3

3 Experimental Methods

3.1 Material Selection

Commercially available 700 µm diameter Ni-rich NiTi wire (NT-E9), supplied by Furukawa Electric Co. Ltd., was used in this study. The wire was thermomechanically processed to exhibit PE properties at room temperature. The composition of these NiTi SMA wires were 50.8 at.% Ni, 49.2% Ti.

3.2 Laser Processing Equipment and Parameters

Laser processing was carried out using a LW50A Miyachi Unitek pulsed Nd:YAG laser system with a 1060 nm wavelength and 600 µm nominal spot size. This system was equipped with a power monitor to allow accurate in situ measurement of incident power output. Monolithic NiTi wires were processed with the top and bottom shielded with argon to avoid oxidation. Argon shielding gas with a flow rate of 0.57 m^3/hr (20 CFH) was used for this study. A wire-processing fixture was used to guide the wire, and an automated wheel was used to control laser processing as shown in **Figure 3-1**.

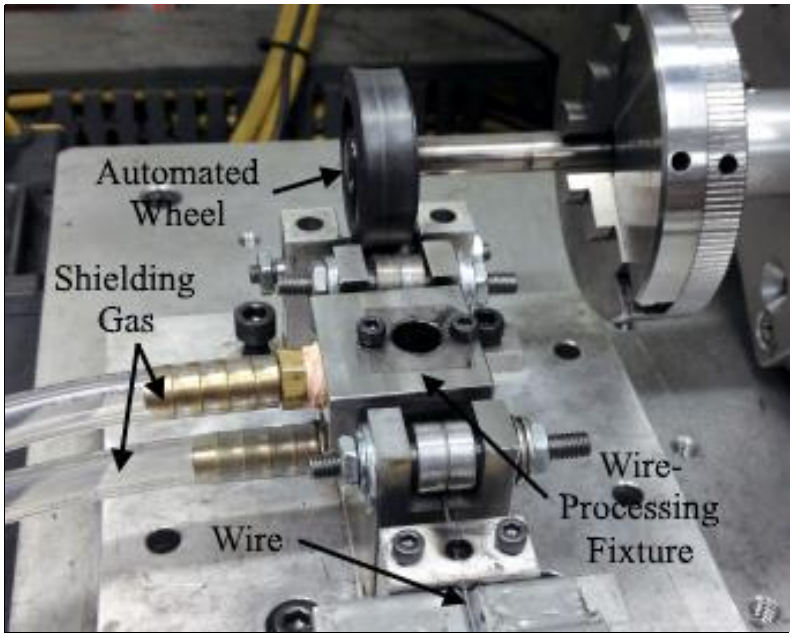

Figure 3-1: LW50A Nd:YAG Laser Processing Setup for NiTi 700 µm wire.

The laser pulse power profile shown in **Figure 3-2** was used for this work to minimize expulsion and solidification cracking while allowing required Ni vaporization for full penetration [86, 87]. A peak power of 2 kW and pulse overlap of 60 % was used to enable full laser penetration and gapless processed region for smooth wire drawing and consistent material properties. The processed and base-material regions in the laser-processed wire are shown in **Figure 3-3**.

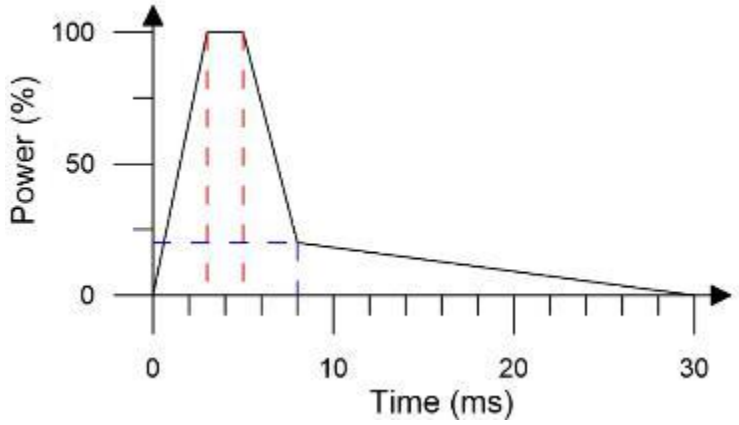

Figure 3-2: Pulsed Nd:YAG Laser Power Profile

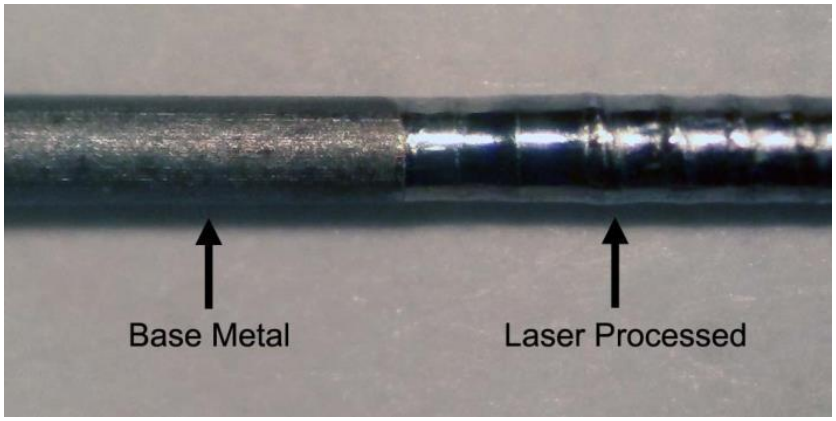

Figure 3-3: NiTi wire base metal and Nd:YAG laser-processed regions [59].

3.3 Post-Processing Thermomechanical Treatment

All treatments performed on the 700 µm NiTi wire along with spring-manufacturing methods are highlighted in this section. Post-processing treatment techniques were adapted from a previous study [59].

3.3.1 Solutionizing

Laser-processed NiTi wires were solutionized in a Carbolite tube furnace with argon atmosphere at 1000 °C for 3600 s, followed by a water quench to homogenize the microstructure for stable wire-drawing. After solutionizing, the wire ends were cut off to avoid excessive build-up of oxides which would lead to breaking during wire-drawing.

3.3.2 Wire-Drawing

The tips of the wires were ground to slender points in order to fit into the dies needed to wire-draw from 700 to 500 µm. The wires were lubricated with MoS_2 thin film lubricant to improve wire drawing quality and lower wire-drawing stresses (see **section 2.4.1: Wire Drawing SMAs**), and allowed to dry for 10 minutes. After lubrication, the die was placed in a vice grip and the tips were pulled through by hand using pliers to allow the sample to be attached to the drawing clamp in the wire drawing setup, shown in **Figure 3-4** [59].

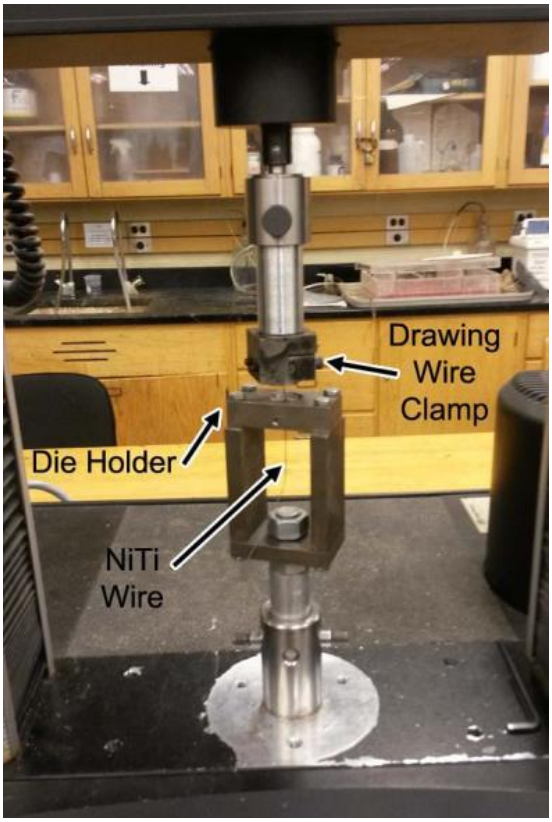

Figure 3-4: Wire drawing setup installed in tensile test machine. Tensile tester used to monitor drawing force and control drawing speed [59].

An Instron 4465 tensile tester was used to control the wire drawing speed, as shown in **Figure 3-4**. A wire-drawing speed of 120 mm/min was used for this work to ensure good wire-drawn quality and uniform wire size reduction. Multiple wire-drawing steps were used to uniformly reduce wire diameter from 700 to 500 µm without breaking the wire, as shown in **Table 3-1**. Inter-annealing was performed after the first wire-drawing step to remove some of the plastic deformation introduced during wire drawing and soften the material for further wire-drawing steps.

Table 3-1: Wire drawing steps post-solutionizing

Die Diameter (µm)	Total Area Reduction (%)
660	11.1
Interanneal 600 °C, 600 s	
620	11.8
580	22.8
540	33.1
500	42.6

Tungsten carbide dies with cobalt matrices, purchased from Advanced Wire Ltd. were used for this study due to superior wear resistance [88]. Since tool steel dies deform relatively quickly, they were avoided to keep die drawing properties consistent throughout the study [88].

3.3.3 Heat Treatment

Cold-worked wires were softened for shape-setting by heat-treating at various temperatures between 400-600 °C (see **section 4.1: Laser Pulse Study** for details) in a pre-heated Thermo Electron Corporation Lindberg/Blue M furnace for 5 minutes. Subsequently, the wires were quenched in cold water to avoid formation of Ni_3Ti (see **section 2.2.4: Heat Treatments**). Tensile test samples were prepared by fixing the wires straight using a shape-setting fixture. Spring samples were made by fixing the wire in a spring shape through a custom spring shape-setting fixture (see **section 3.3.3.1: Spring Shape-Setting Fixture Design and Application**). Finally, the samples were heat-treated at the same temperature as the softening temperature for 55 minutes. DSC samples were taken off the ends of the spring and tensile test samples following final heat treatment.

3.3.3.1 Spring Shape-Setting Fixture Design and Application

Previous attempts at manufacturing helical NiTi springs have resulted in springs with constant diameter [5, 85]. However, these methods do not have the ability to accurately control the pitch of the helical spring. Therefore, a unique universal custom spring fixture (see **Figure 3-5**) was made in this study to fabricate helical compression springs with constant pitches and diameters: 1) pitches ranging from 1.058 mm to 3.175 mm (24 threads per inch (TPI) to 8 TPI), and 2) mean diameters ranging from 4.1 to 7.3 mm.

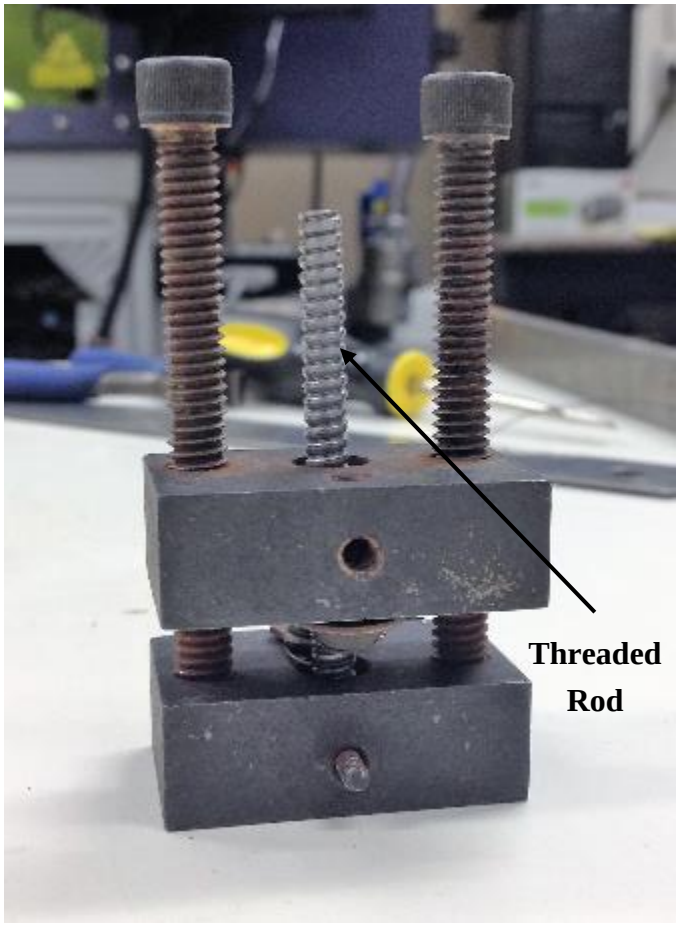

Figure 3-5: Spring shape-setting fixture

A lathe was used to cut out threads in ultra-machinable W1 tool steel. A constant pitch was maintained for each custom threaded rod, and a tapped hole was made at the end to allow the rod to be fixed against the end rectangular block. The rectangular blocks were made using low-carbon steel rectangular bar for relatively easy machining and withstanding high temperatures during

shape-setting. The center hole in the top and end blocks was made to accommodate rod diameters up to 0.3125 in. The wire was held in place by a screw on the end block and wrapped around the custom threaded rod. Once the desired number of coils was achieved, the second rectangular block was lowered down, aligned and fixed to the end block using machine screws. After ensuring the coiled wire was wound tightly around the rod and the ends were secured to the blocks, the machine screws were tightened further to secure the fixture in place and avoid uncoiling the spring during the shape-setting heat treatment, as shown in **Figure 3-5**.

3.4 Analytical Methods

3.4.1 Tensile Test

Tensile tests were carried out using an Instron 5565 table-top visual extensometer equipped with an environmental chamber. Wires of length 52 mm and gauge length 25 mm were required to carry out these tests. White Styrofoam balls were glued to the sample as markers and tracked during each test. This was achieved by skewering the Styrofoam balls as shown in **Figure 3-6 a)**. A two-part epoxy was used to fix the white Styrofoam balls in place and ensure no slipping would occur during the test. Approximately 20 minutes was required for the epoxy to cure before testing the sample. The test setup is illustrated in **Figure 3-6**.

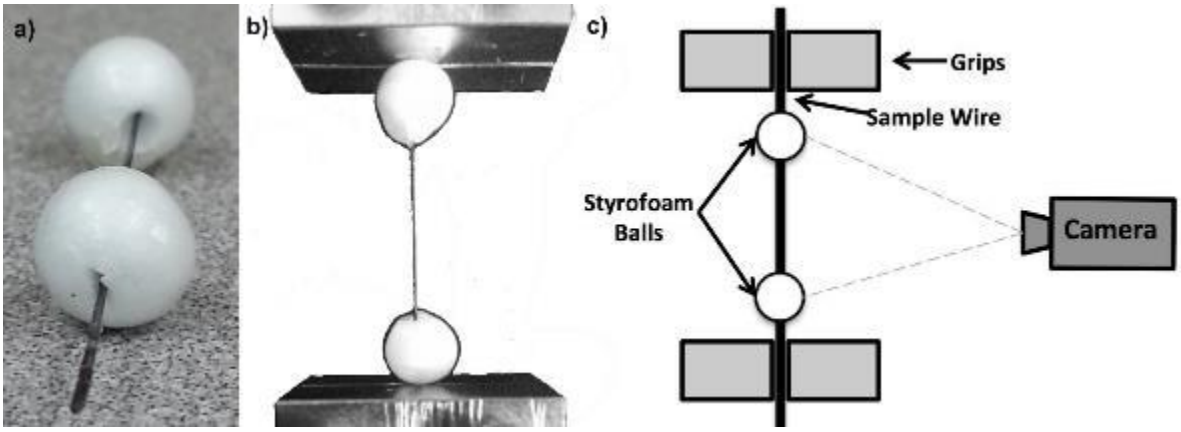

Figure 3-6: Photographs showing a) Styrofoam balls attached to wire sample, b) wire sample loaded in grips with white balls attached and c) schematic depicting the visual extensometer setup [89].

To perform tensile tests at room temperature, each sample was loaded into the top grip of the test chamber, the load was balanced, the sample was positioned in the bottom grip and secured, and

finally, the extension was balanced. A camera attached to the chamber door was used to track the position of the Styrofoam balls (see **Figure 3-6 c)**) during tensile test. Bluehill software on a computer linked to the extensometer was used to run the tensile tests. A tensile test method developed by A. Michael et al. [89] using a strain rate of 0.4 mm/s was used for this work. Pre-cycles were pulled to a strain of 4% before unloading to zero stress.

Tensile tests at higher temperatures were performed to observe stress-strain behaviour of the NiTi sample above A_f, when it is in austenite phase and completely pseudoelastic. The chamber was pre-heated to the required temperature for 1 hour to allow the setup inside the chamber to heat up. Consequently, samples were loaded, balanced and temperatures were allowed to stabilize for about 20 mins before carrying on with the tensile test procedure. Each test case was repeated 3 times with different samples to achieve consistent results.

3.4.2 DSC Test

A Thermal Analysis Q2000 system, equipped with a refrigerated cooling system, was used for Differential Scanning Calorimetry (DSC) analysis. Smaller pieces of wire were cut out from thermo-mechanically processed wires to perform Differential Scanning Calorimetry (DSC) tests. These pieces of wire were placed in a DSC pan, covered with a lid and placed in a slot in the Q2000 system. The ASTM F2004-05 standard was used, with modification of the standard including a test rate of 5 °C min^{-1} and a temperature range of -75 °C to 120 °C [59]. TRIOS software was used to run the tests and analyze the data.

3.4.3 Spring Compression Test

Spring compression tests were performed in an Instron 5548 micro tester equipped with a temperature chamber (-40 °C to 250 °C). NiTi spring samples approximately 1 cm long were used for these experiments. Similar to tensile tests, sets consisting of 3 identical springs were made for repeatability.

Rectangular blocks were fixed at the bottom and top grips of the tensile tester. Springs with grounded ends were placed on the end block, the crosshead was lowered to the spring height, the load was balanced and the gauge length was reset. Then the chamber door was closed and allowed to heat up (for tests at higher temperatures) 10-20 mins, depending on the test temperature. Bluehill

software was used to run the compression tests. Samples were pre-cycled to 2 mm extension before unloading to zero stress.

3.4.4 Stroke Measurement Test

For stroke measurement tests, self-biasing springs consisting of laser-processed (LP) and base material (BM) regions were made using 8TPI custom-threaded rods. To avoid buckling, the springs were preloaded on a screw body in a way such that only the LP region was fully compressed. A white mark was used to indicate the interface between the BM and LP regions and a heat gun was used to heat the spring past the A_f temperature of the LP region. The displacement of the white mark was measured to determine the actuation percentage of the self-biasing spring.

Chapter 4

4 Effects of laser processing and heat treatment on phase transformation temperatures and thermomechanical behaviour of NiTi SMAs

To obtain required functional properties in NiTi, laser-processing and heat treatment parameters need to be modified accordingly (see **section 2.3: Laser Processing Fundamentals** and **section 2.2.4: Heat Treatments**). For this study, the number of laser pulses and heat treatment temperatures were modified to optimize thermal and mechanical properties for NiTi self-biasing springs.

4.1 Laser Pulse Study

A pulse study was carried out to determine maximum separation between phase transformation peaks for multiple memory springs. As-received 700 µm NiTi wires were laser-processed with different number of pulses per spot; thermomechanical treatments were performed to reduce wire diameter to 500 µm (see **section 3.3: Post-Processing Thermomechanical Treatment**); and, a final heat treatment was performed at 400 °C for 1 hour to achieve stable material properties (see **section 2.2.4: Heat Treatments**). DSC plots for BM and multiple-pulse laser-processed wires are shown in **Figure 4-1**.

Martensite was supressed in all of the samples, and R-phase transformation occurred due to the nanocrystalline microstructure [90]. The martensitic transformation peak for the BM sample was not visible because it was located at a temperature lower than the DSC temperature range. Geometric constriction of the matrix by the grain boundaries lead to lower strain intermediate R-phase in forward and reverse transformations [91]. Laser processing removed a significant amount of Ni, which resulted in a shift of transformation temperatures. The peak temperatures for 1 and 2-pulse laser-processed samples were higher because keyhole laser processing resulted in preferential vaporization of Ni (see **section 2.3: Laser Processing Fundamentals**), which lead to reduced Ni concentration in the bulk matrix. Transformation temperatures increased with increasing number of laser pulses due to incremental Ni vaporization [6]. After 2 pulses, the material became Ti-rich and M_s temperatures did not change with additional pulsing due to

insolubility of Ti below 50 at.% Ni (see **section 2.1.5: Physical Metallurgy and NiTi Composition**).

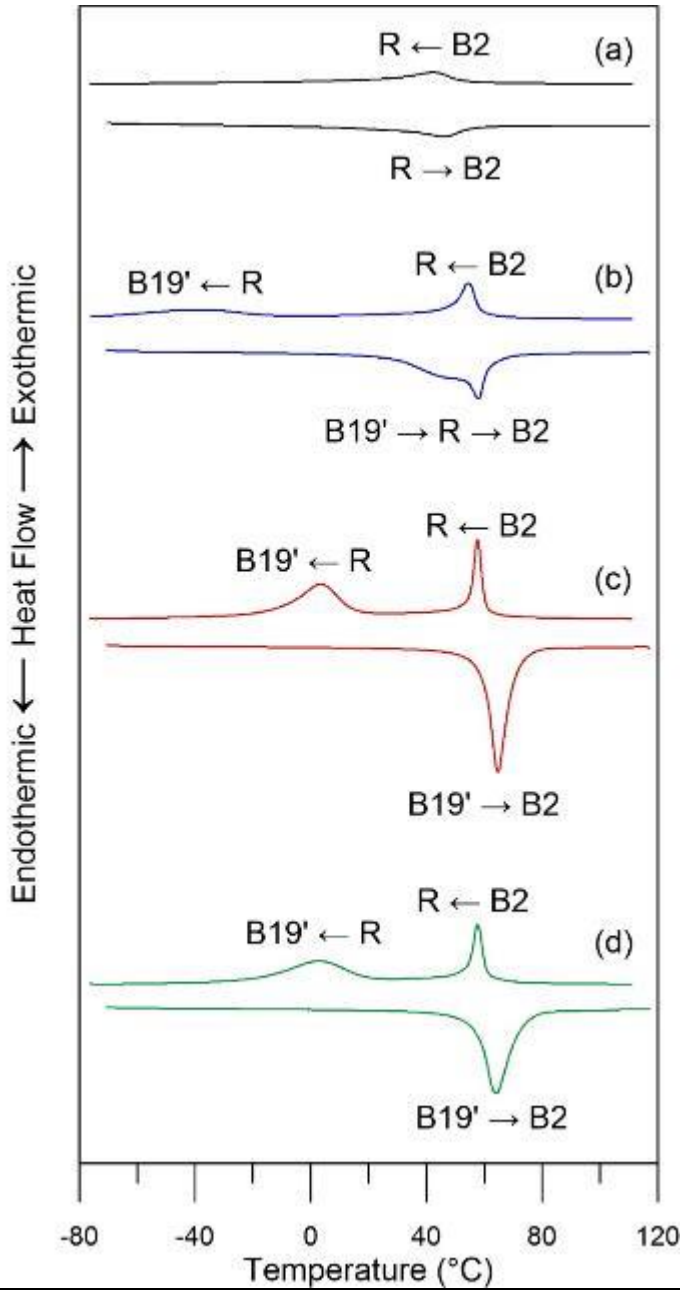

Figure 4-1: DSC curves for cold-worked 500 µm (a) BM, (b) 1-pulse, (c) 2-pulse, and (d) 3-pulse wires heat-treated at 400 °C for 1 hour.

Distinct separation of peaks for each region in a self-biasing spring actuator is necessary to distinguish different memories programmed into a monolithic NiTi material. Heat treatment at 400 °C did not provide sufficient separation as shown in **Table 4-1**, where A_s and A_f are the austenite

start and finish temperatures, and A_p is the peak temperature of austenite phase. Therefore further heat treatments were carried out to study the effect of heat treatment temperature on transformation temperatures.

Table 4-1: Austenitic transformation temperatures for NiTi samples heat-treated at 400 °C

Samples	A_s (°C)	A_p (°C)	A_f (°C)
BM	32.4	46.0	56.1
1P	50.0	58.1	62.0
2P	59.5	64.7	70.8

4.2 Heat Treatment Study

4.2.1 Thermal Characterization

Cold-worked BM, 1 pulse and 2 pulse NiTi wires were heat-treated for 1 hour at 400, 450, 500, 550 and 600 °C respectively, and thermal characterization was performed. The resultant DSC plots are shown in **Figure 4-2**. As heat treatment temperature for base material (BM) increased, the austenite transformation temperatures decreased due to decreased dislocation density and gradual recovery of ordering of the B2 matrix with the progress of precipitation, consistent with the precipitation process [92]. This coincided with the appearance of R↔M transformation. Martensite appeared at 500 °C, and as the temperature increased, R-phase decreased while martensitic transformation peak increased. Above 600 °C, coherent Ti_3Ni_4 precipitates completely dissolved in the B2 matrix, and therefore R-phase disappeared, and single-stream A↔M transformation appeared [92]. Due to the formation of larger incoherent precipitates, the transformation of the Ni-depleted matrix was not affected and this lead to improved matrix uniformity [92].Increasing heat treatment temperatures for Ni-lean NiTi resulted in increased A_f temperatures due to Ni vaporization [6]. Beyond 550 °C, the A_f temperatures for the laser-processed samples did not increase any further as the samples became Ti-rich.

Comparison of DSC plots for different heat treatment temperatures in **Figure 4-2** revealed that heat treatment between 450 °C and 600 °C provided distinct separation between the phase transformation peaks for BM, 1 pulse and 2 pulses. However, heat treatment temperatures above 475 °C do not yield coherent precipitate formation (see **section 2.2.4: Heat Treatments**). Even

though heat treatment at 600 °C for 1 hour may not result in stable material properties [26], a more distinct separation of transformation peaks was achieved. Therefore, further investigations on mechanical properties of 450 °C and 600 °C were carried out to determine the ideal heat treatment temperature for fabricating self-biased spring actuators.

4.2.2 Mechanical Characterization

In addition to thermal characterization, tensile tests were performed to examine the mechanical properties of BM, 1 pulse and 2 pulse samples heat treated at 450 °C (HT_{450}) and 600 °C (HT_{600}) for 1 hour respectively. Stress-strain plots for HT_{450} samples tested at room temperature are shown in **Figure 4-3**. BM had a distinct pseudoelastic plateau which indicated it was PE at room temperature. When the BM sample was strained further, it reached a maximum strain of 6% total strain, and then began to elastically deform. The laser-processed (LP) samples, on the other hand, were not PE at room temperature, which is in agreement with the DSC results. They had much lower stresses during detwinning at room temperature compared to the pseudoelastic plateau of the BM sample. This is desirable for actuation as this indicates that BM is stronger than LP at RT. Ideally, in a self-biasing spring actuator with BM and LP regions, BM would be stronger at lower temperatures and LP would be stronger at higher temperatures ($T>A_{f,LP}$) resulting in spring displacement.

At 600 °C, BM tensile test plot (see **Figure 4-4**) did not recover pseudoelastic strain during unloading which indicated that it was over-annealed and not PE at room temperature. The jaggedness of the plateau region occurred due to the existence of large nanocrystalline grains in the annealed NiTi sample [93]. Furthermore, the UTS of HT_{600} samples was significantly lower than UTS of HT_{450} samples due to more precipitates dissolving at higher temperature.

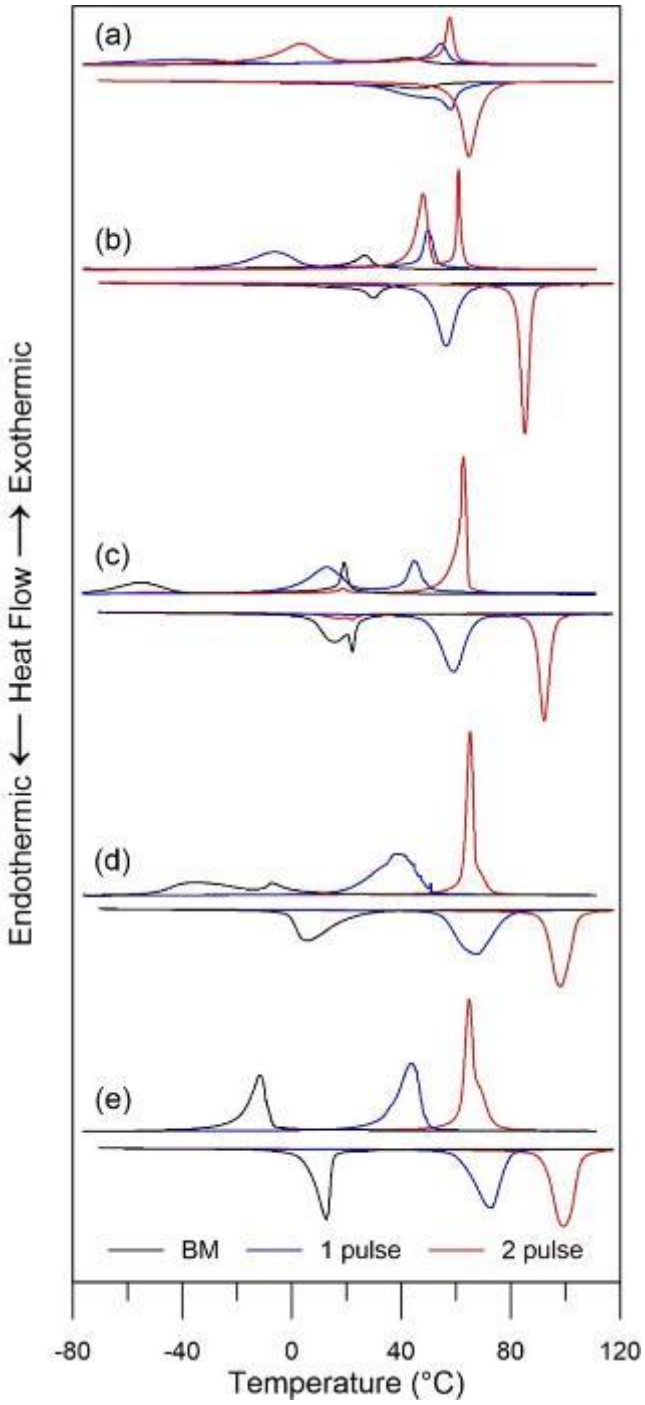

Figure 4-2: DSC curves for cold-worked 500 µm base material, 1-pulse and 2-pulse laser-processed NiTi wires heat-treated at (a) 400 °C, (b) 450 °C, (c) 500 °C, (d) 550 °C, and (e) 600 °C for 1 hour.

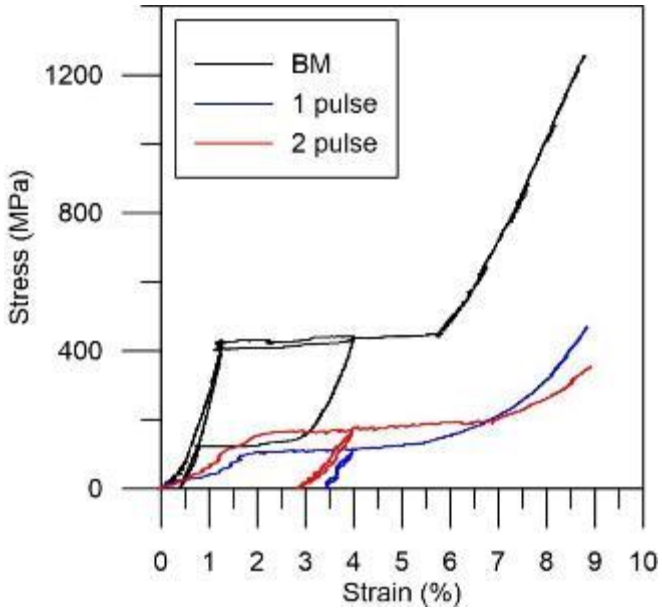

Figure 4-3: Room temperature tensile test plots for BM, 1 pulse and 2 pulse NiTi wires heat treated at 450 °C for 1 hour.

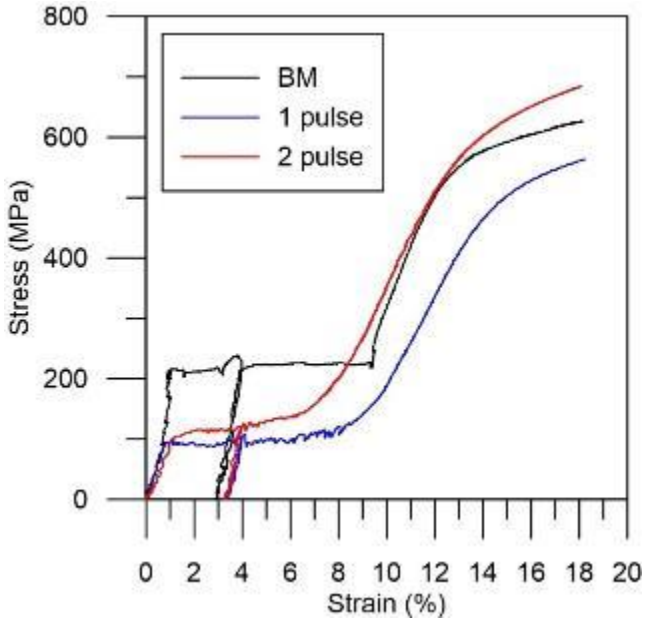

Figure 4-4: Room Temperature tensile test plots for BM, 1 pulse and 2 pulse NiTi wires heat treated at 600 °C for 1 hour.

To further investigate the effect of over-annealing on transformation temperatures, DSC plots of cold-worked samples heat-treated at 1000 °C (solutionized) for 1 hour were studied. DSC plots of solutionized, 450 and 600 °C heat-treated samples are shown in **Figure 4-5**. Cold-working introduced dislocations which are known to suppress martensitic transformation, reducing heat of

transformation [94]. Solutionizing cold-worked samples at 1000 °C for 1 hour (HT_{1000})) removed dislocations and resulted in shallower and wider transformation peaks (see **Figure 4-5 (c)**). This occurred due to heterogeneity in internal stresses, which broadened the range of transformation energy required for complete phase transformation [94, 95].

Both HT_{600} and HT_{1000} samples had single A↔M transformations (see **Figure 4-5 (b) and (c)**), whereas HT_{450} samples had R↔M and M↔A transformations (see **Figure 4-5 (a)**) since Ti_3Ni_4 precipitates were not completely dissolved in the B2 matrix. Also, the transformation temperatures for the laser-processed HT_{1000} samples were similar to the values for HT_{600}, as shown in **Table 4-2**, where the symbols R_p and M_p represent the peak temperatures of R-phase and martensite phase respectively, and R_s, R_f, M_s and M_f represent the start and finish temperatures of R-phase and martensite phase respectively. Solutionized samples are ductile and need to be cold-worked to improve strength, stability and fatigue life (see **section 2.2.3: Cold Working**). Since samples heat-treated at 600 °C show similar attributes to solutionized samples which are ductile at room temperature, they are not suitable for stable actuation.

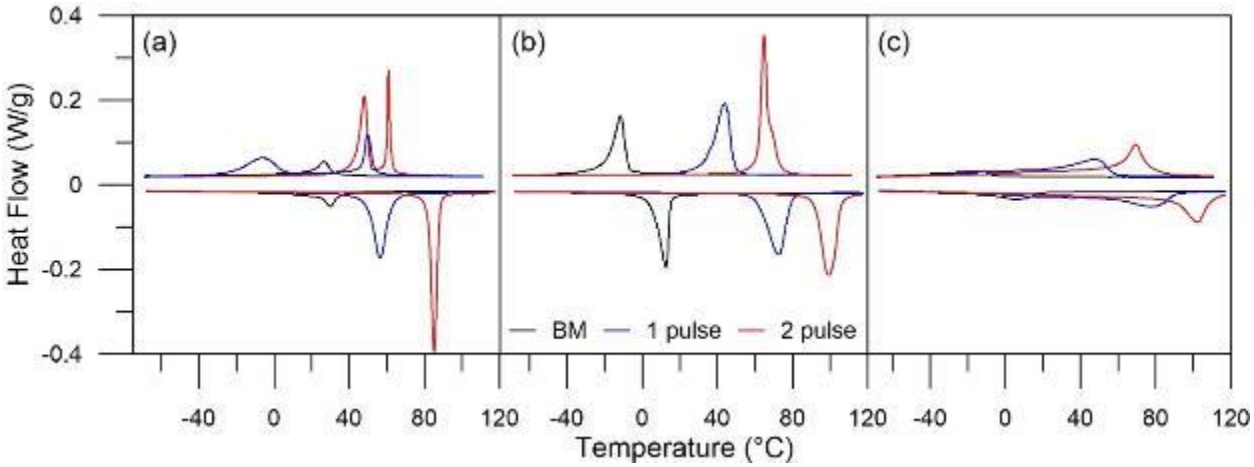

Figure 4-5: DSC curves for cold-worked 500 µm diameter NiTi wires heat-treated at (a) 450 °C , (b) 600 °C, and (c) 1000 °C for 1 hour.

Table 4-2: Transformation temperatures for samples heat treated at 450, 600 and 1000 °C for 1 hour

Sample		A_s (°C)	A_p (°C)	A_f (°C)	R_s (°C)	R_p (°C)	R_f (°C)	M_s (°C)	M_p (°C)	M_f (°C)
HT_{450}	**BM**	24.6	30.1	34.7	31.6	26.4	20.8	-	-	-
	1P	49.8	56.5	62.4	53.4	49.7	46.9	5.9	-6.3	-22.9
	2P	82.1	85.3	88.0	62.1	60.9	60.0	51.1	47.9	43.3
HT_{600}	**BM**	5.3	12.7	14.9	-	-	-	-8.6	-11.8	-18.8
	1P	61.0	72.8	79.4	-	-	-	48.9	43.9	34.5
	2P	92.1	99.5	105.7	-	-	-	67.8	64.8	61.7
HT_{1000}	**BM**	-12.5	5.3	18.5	-	-	-	-5.0	-16.1	-47.5
	1P	51.5	77.2	86.6	-	-	-	57.5	47.9	20.8
	2P	90.9	102.2	108.9	-	-	-	76.3	69.3	60.9

4.3 Chapter Summary

In summary, pulse study and heat treatment study were performed to determine the maximum number of memories with the current laser pulse profile and the optimum set of parameters for post-processing. Samples laser-processed beyond 2 pulses became Ti-rich and brittle due to vaporization of Ni, allowing for a maximum of three different compositions in one actuator. From heat-treatment study, it was determined that samples heat-treated at 450 °C and 600 °C show distinct separation between BM, 1-pulse and 2-pulse peaks. Tensile test results revealed that the BM samples heat treated at 600 °C were over-annealed at room temperature and therefore not pseudoelastic. The pseudoelastic strain for BM heat-treated at 450 °C was recoverable at room temperature, and the heat treatment temperature promoted good nucleation and diffusion for fine precipitate formation. Therefore, a final heat treatment temperature of 450 °C was chosen to optimize the self-biased spring actuator properties.

Chapter 5

5 Effect of spring geometry on mechanical properties of NiTi spring and self-biased spring actuation

5.1 Spring Geometry Study

In this part of the study, mechanical properties of compression springs with ground ends were determined by measuring their stress-strain behaviour upon compression. NiTi springs with different diameters and pitches were tested to determine the effect of spring geometry on actuation. The geometric parameters used in the following subsections include the average number of active coils, N_a, average mean spring diameter, D, and spring pitch, p. A set of 3 springs was used to determine the average geometric and experimental values as discussed in **section 3.4.3: Spring Compression Test**. For each spring, L_f<4D condition was maintained to avoid buckling.

5.1.1 Different Diameters

The force exerted by a spring is strongly dependent on spring diameter as shown in **Equation (2-5)**. To verify if this equation holds true for NiTi springs, compression tests of two BM springs WD1 (with D ≈ 7.3 mm and p = 24 TPI) and SD1 (with D ≈ 4.1 mm and p = 24 TPI) were performed as shown in **Figure 5-1**. The experimental force, F_{exp}, was determined from the average force obtained from stress-strain curves at 2 mm extension. The theoretical force, F_{th}, was calculated by using derived **Equation (5-1)**, where the actual spring displacement, δ_{act}, was at an experimental extension of 2 mm, the shear modulus of elasticity, G, was 26300 N/mm^2 and the wire diameter, d, was 0.49 mm. The ratios R_{exp} and R_{th}, which represent the experimental ratio of forces and theoretical ratio of forces, were calculated using Equations **(5-2)** and **(5-3)**. As the spring diameter decreased by 0.56 from WD1 to SD1, the experimental force increased by 4.25 ($R_{exp,SD1}$) at 45 °C. The theoretical force increased by approximately D_{WD1}^3/D_{SD1}^3 which translates to 5.22. However, correcting for N_a, the theoretical force increased by $(N_{a,WD1}*D_{WD1})/(N_{a,SD1}*D_{SD1})$ which equates to a value of 4.69 ($R_{th,SD1}$), as shown in **Table 5-1**. This result corresponds well with the experimental ratio $R_{exp,SD1}$.

$$F_{th} = \frac{Gd\delta_{act}}{D^3 N_a} \tag{5-1}$$

$$R_{exp} = \frac{F_{exp,SD1}}{F_{exp,WD1}} \tag{5-2}$$

$$R_{th} = \frac{F_{th,SD1}}{F_{th,WD1}} \tag{5-3}$$

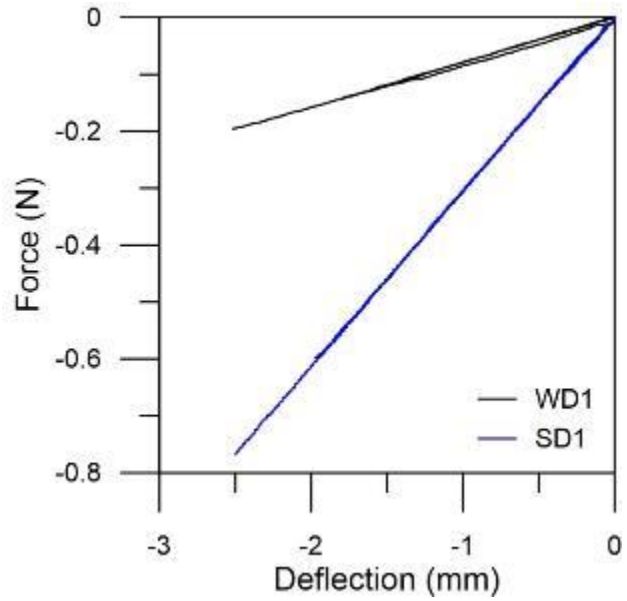

Figure 5-1: Compression test results for small-pitch (1.08 mm) large (7.3 mm) and small (4.1 mm) diameter NiTi springs taken at 45 °C

Table 5-1: Comparison of theoretical and experimental spring rate ratios for springs with different diameters and pitches.

Spring	N_a	D (mm)	p (TPI)	F_{th} (N)	F_{exp} (N)	R_{th}	R_{exp}
WD2	4.44	7.05	18	0.24	0.27	1.81	1.74
WD1	6.86	7.44	24	0.13	0.15	1	1
SD1	7.62	4.29	24	0.63	0.65	4.69	4.25
SD2	4.75	4.15	16	1.11	1.25	1.76	1.92
SD3	2.68	3.99	8	2.16	3.21	1.95	2.57

5.1.2 Different Pitches

To observe the effect of pitch on the mechanical behaviour of the NiTi compression springs, compression tests were performed for large and small diameter springs with different pitches as shown in **Figure *5-2***. Springs WD1 and WD2 had larger diameter compared to SD1, SD2 and SD3, but WD2 had a larger pitch (18 TPI) compared to WD1. Smaller diameter springs SD2 and SD3 had identical diameters but different pitches compared to SD1. For the large diameter springs,

when the pitch increased by 1.33, the experimental force increased by 1.74 ($R_{exp,WD2}$). Theoretically, when the spring pitch increased from WD1 to WD2, the force should have increased by $N_{a,WD1}/N_{a,WD2}$ which yields a value of 1.55. However, correcting for D, the force increased by $(N_{a,WD1}*D_{WD1}^3)$ $/(N_{a,WD2}*D_{WD2}^3)$ which equates to 1.81 ($R_{th,WD2}$), relatively close to $R_{exp,WD2}$. Similarly, for the small diameter springs, the force increased by 1.76 experimentally and 1.92 theoretically as pitch increased by 1.5 from SD1 to SD2. When the pitch doubled from SD2 to SD3, the corresponding theoretical and experimental ratios were 1.95 and 2.57 respectively.

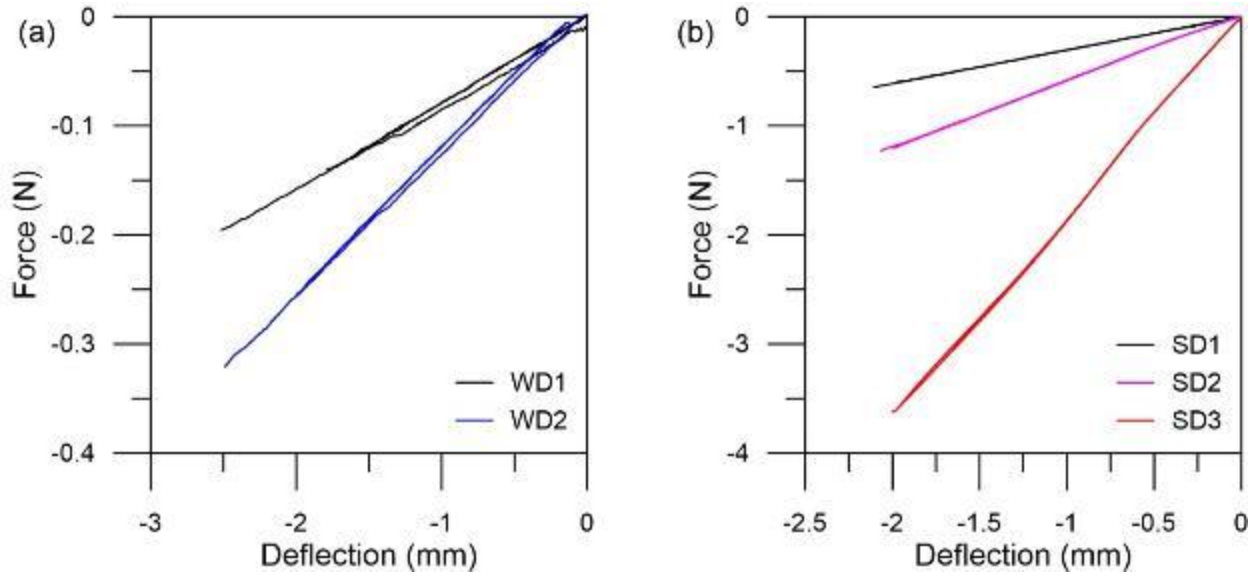

Figure 5-2: Compression test results for different-pitch (a) large (7.3 mm) and (b) small (4.1 mm) diameter NiTi springs taken at 45 °C

Overall, it was observed that the experimental values agree with the theoretical values, which indicates that BM NiTi springs behave as regular springs in austenite phase. With the wire diameter constant at 0.49 mm, the spring with the largest pitch and smallest diameter produced the largest force both theoretically and experimentally. The relatively larger difference between R_{th} and R_{exp} for the 8TPI spring was most likely due to the larger pitch angle, which likely lead to inaccurate compression test measurements.

5.2 Thermomechanical Analysis of 8TPI Springs

Since the BM small diameter 8TPI springs generated the largest force at 45 °C, BM, 1P and 2P 8TPI springs were tested at RT, 45 °C, 80 °C and 110 °C respectively to determine the

thermomechanical characteristics (see **Figure 5-3**). At RT, all samples were detwinning. As the temperature increased to 45 °C, BM transformed to austenite phase and became elastic. When the temperature increased to 80 °C, 1P transformed to austenite phase and both 1P and BM were elastic. At 110 °C, the spring rate for the 2P spring increased significantly as it completely transformed to austenite. However, it was still slightly weaker than the BM and 1P springs as observed in **Figure 5-3 d)**, possibly due to changes in composition.

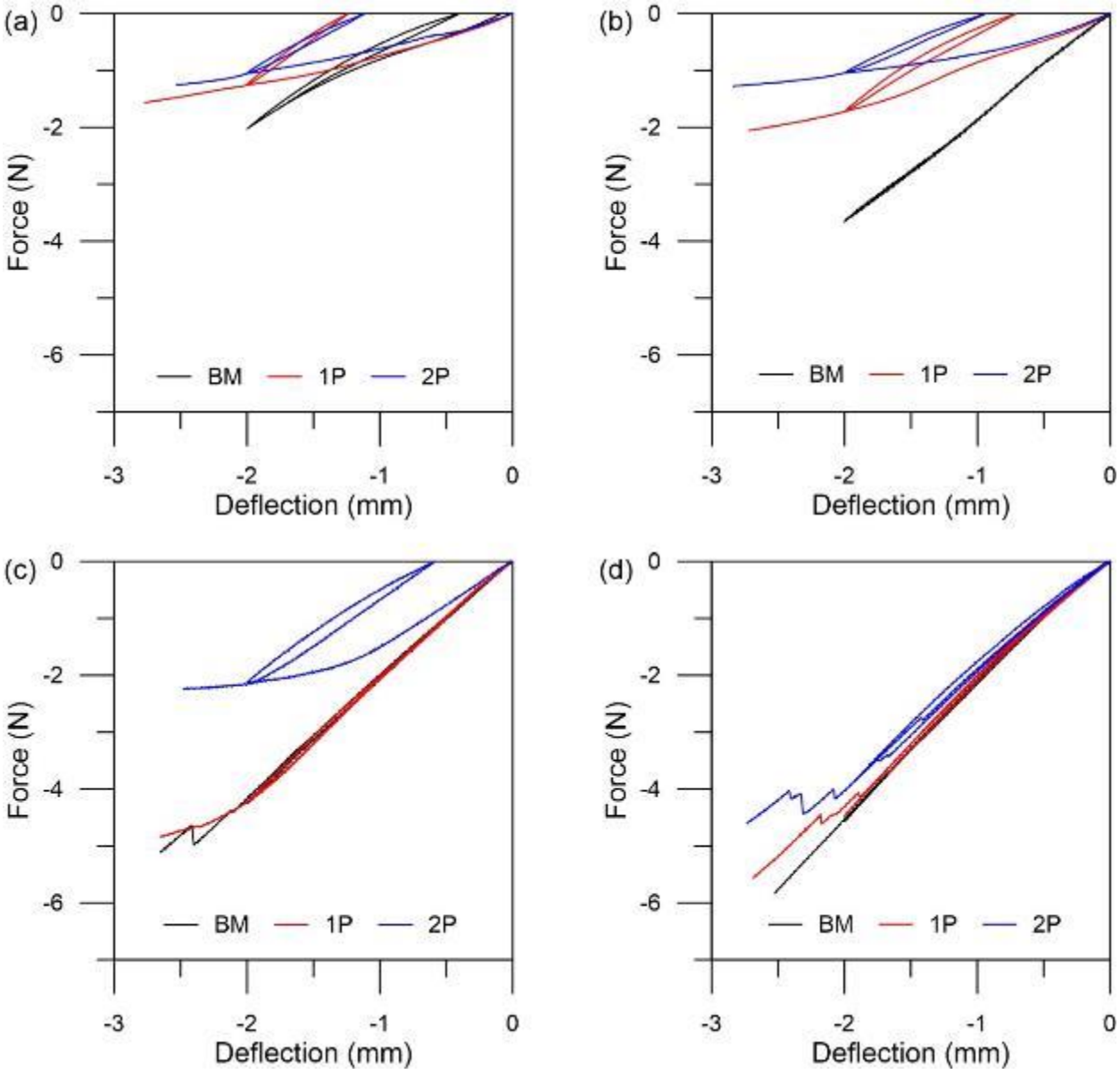

Figure 5-3: Compression test results for BM, 1P and 2P 8TPI springs taken at (a) RT, (b) 45 °C, (c) 80 °C and (d) 110 °C.

5.3 Self-Biasing Spring Stroke

5.3.1 Theoretical Calculation

Using the compression test results from **Figure 5-3**, an 8TPI self-biasing spring geometry of 6 1P coils and 6 BM coils was determined to provide sufficient stroke for actuation. Calculation of stroke was performed by comparing 4 plots – BM 45 °C, 1P 45 °C, BM 80 °C and 1P 80 °C – as illustrated in **Figure 5-4**. Experimental data for N_a of BM and 1P springs was scaled up from approximately 3 to 6 coils. The corresponding experimental data for extension was scaled up by approximately 2 since N_a is directly proportional to extension. The maximum compression of 1P and corresponding compression of BM at matching force required to compress 1P was determined. A difference in compression of approximately 5.6 mm was observed. Heating the preloaded self-biasing spring to 80 °C increases the force of the 1P spring. The BM and 1P sections of the spring balance force and extension. Therefore, the interface between 1P and BM should move approximately 2.8 mm when heated to 80 °C. This is the theoretical stroke of the preloaded SB spring.

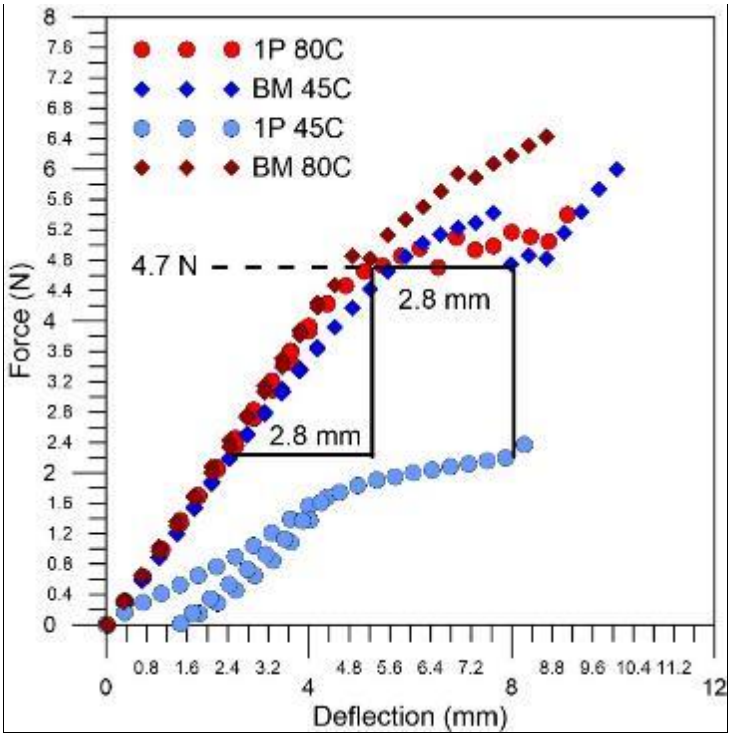

Figure 5-4: Calculation of stroke from compression stress-strain plots of BM and 1P samples at 45 °C and 80 °C respectively.

5.3.2 Experimental Characterization

A self-biasing (SB) spring with 12 coils (approximately 6 1P coils and 6 BM coils) was made and tested as shown in **Figure 5-5**. The spring was compressed to a length (2.1 cm) at which the 1P laser-processed region (left-section) was almost fully compressed and the BM region was not (**Figure 5-5 a)**). The white mark, denoting the interface between the 1P and BM regions, was initially at approximately 1.6 mm. However, after application of heat with a heat gun, the white mark moved to approximately 1.2 mm (**Figure 5-5 b)**).

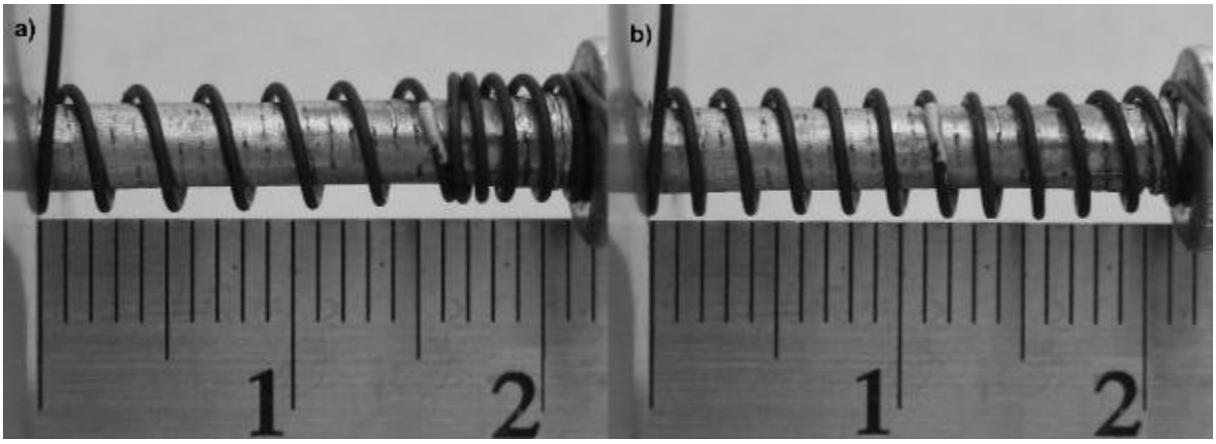

Figure 5-5: Displacement of pre-loaded 1-memory self-biased spring tested by heating with a heat gun. The section of the spring with compressed coils is the 1P laser-processed region, and the white mark indicates the start position of the 1P region. Position (a) represents position with no heat applied, and (b) represents position with heat applied beyond A_f of the 1P region.

A displacement of 4 mm (19% actuation) was achieved as the SB spring was heated above the A_f of the 1P region. Also, since 1P was as strong as BM in austenite phase, the spring balanced itself out as observed by the consistent spring pitch in **Figure 5-5 b)**. However, the experimental stroke was even higher than the theoretical stroke calculated in the previous section. This may be because the number of active BM and 1P coils were not exactly 6 each respectively.

To further enhance the actuation characteristics of the SB spring, a monolithic 3-memory SB spring with BM, 1P and 2P sections was made. The spring was compressed to a length at which the 1P and 2P regions were almost fully compressed (2.4 cm). From left to right in **Figure 5-6 a)**, the spring consisted of approximately 2.5 2P laser-processed coils, 3.5 1P laser-processed coils and 6 BM coils. When the spring was heated above the A_f of the 1P region, the white mark moved approximately 1 mm. Further heating past the A_f of the 2P coils resulted in a displacement of 2

mm and a total displacement of 3 mm (12.5% actuation). Consistent pitch is not seen throughout the spring because 2P has a lower spring constant than 1P and BM, as seen in **Figure 5-3**.

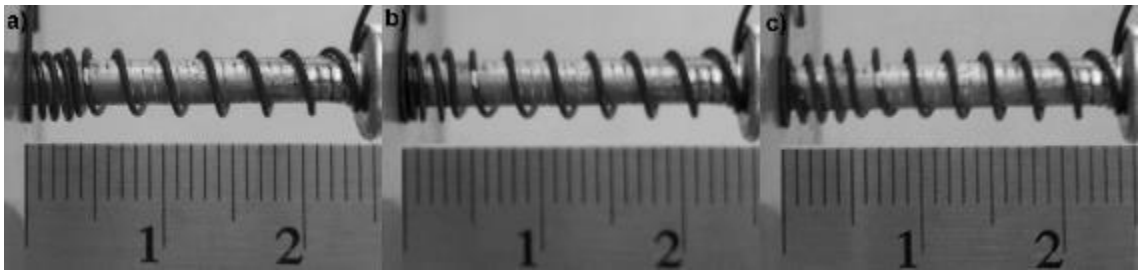

Figure 5-6: Displacement of pre-loaded 3-memory self-biased spring tested by heating with a heat gun. The section of the spring with compressed coils consists of the 1P and 2P laser-processed regions, and the white mark indicates the start position of the 1P region. Position (a) represents position with no heat applied, (b) represents position with heat applied beyond Af of the 1P region, and (c) represents position with heat applied beyond A_f of 2P region.

5.4 Chapter Summary

In summary, NiTi spring forces increased with increasing pitch and decreased with increasing mean spring diameter for springs with identical wire diameters. The spring with the smallest diameter and largest pitch was chosen as the strongest spring for the self-biased spring. From the compression test results, it was shown that BM was stronger than 1P and 2P at 45 °C, 1P was stronger than 2P at 80 °C, and 2P was austenitic but slightly weaker than BM and 1P at 110 °C. The single-memory SB spring actuated when the spring was heated above the A_f of 1P to displace the spring by 4 mm. Adding 1 more memory in the SB spring showed different actuation characteristics as the spring was heated to 2 different temperatures to observe movement of the 1P and 2P regions. A total actuation of 12.5% was achieved thorough this mechanism.

Chapter 6

6 Conclusions and future work

The purpose of this work was to determine laser processing and heat treatment parameters ideal for making and characterizing self-biased NiTi spring actuators. Consequently, a laser pulse study was performed to study the shift in transformation temperatures for optimizing actuation. Similarly, a heat treatment study was used to investigate the effect of temperature on separation between multiple transformation peaks. In addition, a spring geometry study was performed to determine ideal diameter and pitch required for manufacturing self-biased springs. Stroke measurement theoretical and experimental studies were performed to determine the magnitude of actuation achieved with a self-biased spring. The following sections contain the major conclusions of this thesis and recommendations for future work.

6.1 Conclusions

6.1.1 Laser Processing and Heat Treatment Study

For the first part of this study, DSC characterization was performed for cold-worked NiTi samples laser processed with different number of pulses and heat treated at 400 °C for 1 hr. The second part of the study involved thermomechanical characterization of samples heat-treated at different temperatures between 400 and 600 °C. The main findings of this study are as follows:

1. Increasing the number of laser pulses beyond 2 resulted in Ti-rich NiTi samples.
2. Thermomechanical characterization proved that final heat treatment temperature of 450 °C produced distinct BM, 1-pulse and 2-pulse phase transformation.

6.1.2 Spring Geometry and Self-Biased Spring Actuation Study

Using a shape-setting temperature of 450 °C, springs with different diameters and pitches were made to study the effect of spring geometry on thermomechanical properties. These results were used to manufacture self-biased springs. The following major conclusions were drawn from the study:

1. Relationship between spring geometries and force exerted conforms to established equations.

2. A spring geometry of 8TPI (3.175 mm) and approximately 4.1 mm mean diameter was determined to generate the highest spring force of those tested.
3. A total displacement of 4 mm (19 % actuation) was observed when the preloaded 1-memory SB spring was heated above the A_f of the 1P laser-processed region.
4. With the inclusion a 2P region in the SB spring, 2-stage actuation was observed with the first and second stage yielding actuation of about 1 mm and 2 mm respectively. A total actuation of 12.5 % was achieved through this mechanism.

6.2 Recommendations for Future Work

6.2.1 Additional Memories

Laser-processing allows for the integration of multiple memories in a monolithic NiTi material as observed by Khan et al. [6]. In this study, 3 memories were programmed into a monolithic NiTi spring to demonstrate 2-stage actuation. Adding additional memories to the spring by optimizing laser processing parameters would enable multi-stage actuation. This would open the doors to numerous potential applications while reducing costs as fewer equipment would be required for the spring actuator.

6.2.2 Optimizing Spring Geometry to Achieve Maximum Stroke

Diameter and pitch of the spring strongly affect the spring rate as observed in this work. However, different ratio of BM coils to LP coils or compression spring with non-uniform geometries were not tested. The spring stroke could vary significantly if different shapes of compression springs were used as shown in **Figure 6-1**. For instance, instead of constant-diameter springs, conical springs could be used to increase the maximum stroke. In a 2-memory SB spring, 1P laser-processed region could be programmed in the tapered end of the spring and BM could be mapped in the wider section of the spring. Wider coil diameter for the BM section of the spring would lead to decreased forces at austenite, while 1P section would likely be stronger at austenite due to smaller coil diameter. Heating the preloaded spring would likely result in a larger displacement of the 1P region due to increased spring rate, thus resulting in increased actuation.

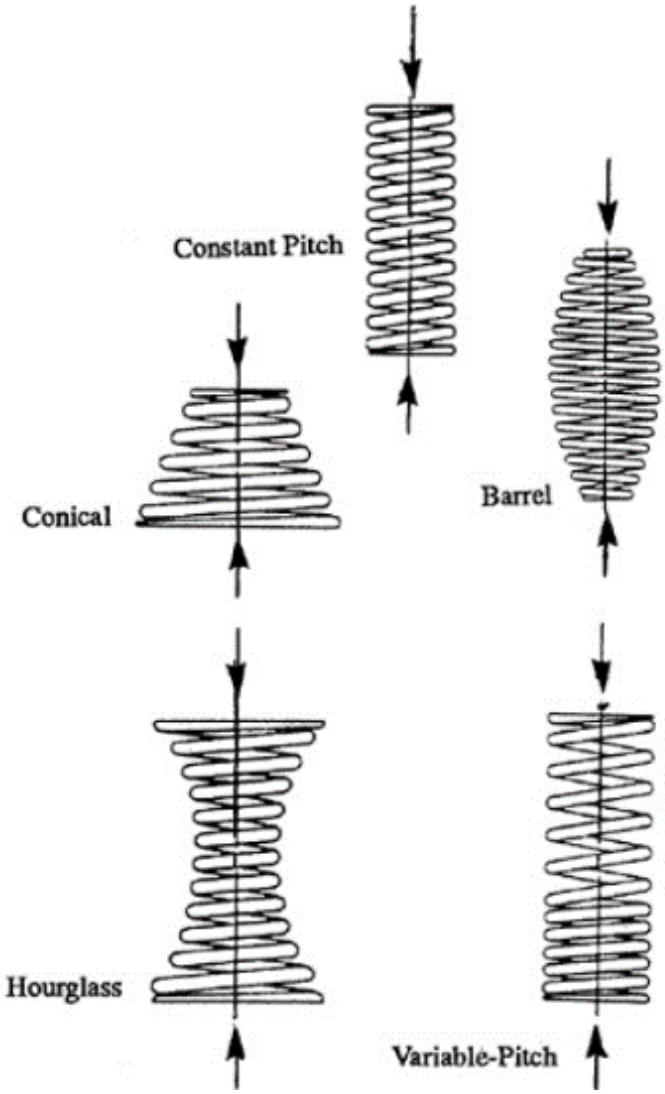

Figure 6-1: Different Compression Spring Geometries [75].

A similar self-biasing mechanism can be applied for the hourglass and barrel-shaped compression springs. For the hourglass spring, incorporating the 1P region in the narrow section and base material in the wider sections of the spring would lead to two-way actuation. The laser-processed region would displace towards either end of the preloaded hour glass spring and higher actuation can be generated by adjusting the LP to BM coil ratio. On the contrary, barrel-shaped compression springs would need to have 1P laser-processed regions at either end of the spring and BM in the middle for self-biased actuation. Since the 1P sections of the spring would be stronger than BM at A_f of 1P, the preloaded spring would be pushed inwards when heated above the corresponding temperature.

6.2.3 Tension Springs

In this work, only compression springs were used due to the simplicity of manufacturing. However, tension springs could potentially achieve higher actuation in a self-biasing mechanism. Studies for NiTi helical extension springs with different dimensions have been shown to generate large amounts of net strain [85]. Since the maximum stroke of the spring is strongly dependent on net strain, increasing the net strain, while keeping free length of the spring constant, would most likely increase the maximum stroke of the SB spring.

References

[1] W. J. Buehler, J. V. Gilfrich, and R. C. Wiley, "Effect of Low-Temperature Phase Changes on the Mechanical Properties of Alloys near Composition TiNi," *Journal of Applied Physics,* vol. 34, pp. 1475-1477, 1963.

[2] J. M. Jani, M. Leary, A. Subic, and M. A. Gibson, "A review of shape memory alloy research, applications and opportunities," *Materials & Design,* vol. 56, pp. 1078-1113, 2014.

[3] D. Stoeckel, "Shape Memory Actuators Improve Car Performance," *Springs,* vol. 31, May 1992.

[4] D. Stoeckel, "Shape memory actuators for automotive applications," *Materials & Design,* vol. 11, pp. 302-307, 1990.

[5] M. Follador, M. Cianchetti, A. Arienti, and C. Laschi, "A general method for the design and fabrication of shape memory alloy active spring actuators," *Smart Materials and Structures,* vol. 21, p. 115029, 2012.

[6] M. I. Khan, A. Pequegnat, and Y. N. Zhou, "Multiple Memory Shape Memory Alloys," *Advanced Engineering Materials,* vol. 15, pp. 386-393, 2013.

[7] K. Otsuka, T. Sawamura, and K. Shimizu, "Crystal structure and internal defects of equiatomic TiNi martensite," *physica status solidi (a),* vol. 5, pp. 457-470, 1971.

[8] G. Fan, W. Chen, S. Yang, J. Zhu, X. Ren, and K. Otsuka, "Origin of abnormal multi-stage martensitic transformation behavior in aged Ni-rich Ti–Ni shape memory alloys," *Acta Materialia,* vol. 52, pp. 4351-4362, 2004.

[9] J. A. Shaw, C. B. Churchill, M. A. Iadicola, "Tips and tricks for characterizing shape memory alloy wire: Part 1 – Differential scanning calorimetry and basic phenomena," *Experimental Techniques*, vol. 32, pp. 55-62, 2008.

[10] G. B. Kauffman and I. Mayo, "The Story of Nitinol: The Serendipitous Discovery of the Memory Metal and Its Applications," *The Chemical Educator,* vol. 2, pp. 1-21, 1997.

[11] C. P. Frick, A. M. Ortega, J. Tyber, A. E. M. Maksound, H. J. Maier, Y. Liu, *et al.*, "Thermal processing of polycrystalline NiTi shape memory alloys," *Materials Science and Engineering A,* vol. 405, pp. 34-49, 2005.

[12] B. Tam, "Micro-Welding of Nitinol Shape Memory Alloy," MASc Thesis, University of Waterloo, Waterloo, ON, Canada, 2010.

[13] M. H. Elahinia, M. Hashemi, M. Tabesh, and S. B. Bhaduri, "Manufacturing and processing of NiTi implants: A review," *Progress in Materials Science,* vol. 57, pp. 911-946, 2012.

[14] J. Wang, "Multiple Memory Material Processing for Augmentation of Local Pseudoelasticity and Corrosion Resistance of NiTi-based Shape Memory Alloys," MASc Thesis, Mechanical Engineering, University of Waterloo, Waterloo, ON, Canada, 2013.

[15] K. Bhattacharya, *Microstructure of martensite : Why it Forms and how it gives rise to the shape-memory effect*. New York: Oxford University Press, 2003.

[16] K. O. M. Piao, S. Miyazaki, H. Horikawa, "Mechanism of the As temperature increase by pre-deformation in thermoelastic alloys," *Materials Transactions, Japan Institute for Materials,* vol. 34, p. 919, 1993.

[17] R. F. Hamilton, H. Sehitoglu, Y. Chumlyakov, and H. J. Maier, "Stress dependence of the in single crystal NiTi alloys," *Acta Materialia,* vol. 52, pp. 3383-3402, 2004.

[18] T. H. Nam, T. Saburi, K. Shimizu, "Cu-Content Dependence of Shape Memory Characteristics in Ti-Ni-Cu Alloys," *Materials Transactions, JIM,* vol. 31, pp. 959-967, 1990.

[19] E. Hornbogen, "Surface upheavals, pseudo martensite, and martensite ghosts," *Practical Metallography,* vol. 42, pp. 445-453, 2005.

[20] S. Miyazaki, "Martensitic transformation in TiNi alloys," in *Thin Film Shape Memory Alloys: Fundamentals and Device Applications*, W. M. H. S. Miyazaki, Y.Q. Fu, Ed., ed: Cambridge University Press & Science Press, 2009, pp. 73-87.

[21] Y. Liu, Z. Xie, J. Van Humbeeck, L. Delaey, "Some results on the detwinning process in NiTi shape memory alloys," *Scripta Materialia,* vol. 41, pp. 1273-1281, 1999.

[22] ASTM F2004-05, "Standard Test Method for Transformation Temperature of Nickel-Titanium by Thermal Analysis," ed. West Conshohocken, PA ASTM International, 2009.

[23] K. Otsuka and K. Shimizu, "Pseudoelasticity and shape memory effects in alloys," *International Metals Reviews,* vol. 31, pp. 93-114, 1986.

[24] A. R. Pelton, J. Dicello, and S. Miyazaki, "Optimisation of processing and properties of medical grade Nitinol wire," *Minimally Invasive Therapy & Allied Technologies,* vol. 9, pp. 107-118, 2000.

[25] K. O. S. Miyazaki, Y. Suzuki, "Transformation pseudoelasticity and deformation behavior in a Ti-50.5at%Ni alloy," *Scripta Metallurgica* vol. 15, p. 287, 1981.

[26] K. Otsuka and X. Ren, "Physical metallurgy of Ti–Ni-based shape memory alloys," *Progress in Materials Science,* vol. 50, pp. 511-678, 2005.

[27] M. I. Khan, "Pulsed Nd:YAG Laser Processing of Nitinol," PhD Thesis, Mechanical Engineering, University of Waterloo, Waterloo, ON, Canada, 2011.

[28] W. Tang, "Thermodynamic study of the low-temperature phase B19′ and the martensitic transformation in near-equiatomic Ti-Ni shape memory alloys," *Metallurgical and Materials Transactions A,* vol. 28, pp. 537-544, 1997.

[29] S. Miyazaki, Y. Ohmi, K. Otsuka, and Y. Suzuki, "Characteristics of deformation and transformation pseudoelasticity in ti-ni alloys," *J. Phys. Colloques,* vol. 43, pp. C4-255-C4-260, 1982.

[30] D. Hodgson and S. Russell, "Nitinol melting, manufacture and fabrication," *Minimally Invasive Therapy & Allied Technologies,* vol. 9, pp. 61-65, 2000.

[31] N. Morgan, A. Wick, J. Dicello, R. Graham, "Carbon and oxygen levels in nitinol alloys and the implications for medical device manufacture and durability," in *Proceedings of the International Conference on Shape Memory and Superelastic Technologies*, Pacific Grove, California, 2006, pp. 821-828.

[32] J. Frenzel, J. Pfetzing, K. Neuking, and G. Eggeler, "On the influence of thermomechanical treatments on the microstructure and phase transformation behavior of Ni–Ti–Fe shape memory alloys," *Materials Science and Engineering: A,* vol. 481–482, pp. 635-638, 2008.

[33] R. Kocich, I. Szurman, M. Kursa, and J. Fiala, "Investigation of influence of preparation and heat treatment on deformation behaviour of the alloy NiTi after ECAE," *Materials Science and Engineering: A,* vol. 512, pp. 100-104, 2009.

[34] H. Mirzadeh and M. H. Parsa, "Hot deformation and dynamic recrystallization of NiTi intermetallic compound," *Journal of Alloys and Compounds,* vol. 614, pp. 56-59, 2014.

[35] M. H. Wu, "Fabrication of nitinol materials and components," in *Proceedings of the International Conference on Shape Memory and Superelastic Technologies (SMST)*, pp. 285-291, 2001.

[36] A. Tuissi, P. Bassani, A. Mngioni, L. Toia, F. Butera, "Fabrication process and characterization of NiTi wires for actuators," SAES Getters, Milano, Italy, 2004.

[37] S. D. Prokoshkin, I. Y. Khmelevskaya, V. Brailovski, F. Trochu, S. Turenne, and V. Y. Turilina, "Thermomechanical Treatments and Their Influence on the Microstructure and Stress/Strain Diagrams of NiTi Shape Memory Alloys," *Canadian Metallurgical Quarterly,* vol. 43, pp. 95-108, 2004.

[38] Z. Lekston, M. Zubko, K. Prusik, and D. Stróż, "Microstructure, Phase Transformations, and Properties of Hot-Extruded Ni-Rich NiTi Shape Memory Alloy," *Journal of Materials Engineering and Performance,* vol. 23, pp. 2362-2367, 2014.

[39] E. Hornbogen, "Ausforming of NiTi," *Journal of Materials Science,* vol. 34, pp. 599-606, 1999.

[40] D. Treppmann and E. Hornbogen, "On the Influence of Thermomechanical Treatments on Shape Memory Alloys," *J. Phys. IV France,* vol. 07, pp. C5-211-C5-220, 1997.

[41] J. C. Ewert, I. Böhm, R. Peter, and F. Haider, "The role of the martensite transformation for the mechanical amorphisation of NiTi," *Acta Materialia*, vol. 45, pp. 2197-2206, 1997.

[42] D. Wurzel, "Effects of different thermomechanical treatments on fatigue of NiTi shape memory alloys," *J. Phys. IV France*, vol. 11, pp. Pr8-535-Pr8-540, 2001.

[43] K. Gall, J. Tyber, G. Wilkesanders, S. W. Robertson, R. O. Ritchie, and H. J. Maier, "Effect of microstructure on the fatigue of hot-rolled and cold-drawn NiTi shape memory alloys," *Materials Science and Engineering: A*, vol. 486, pp. 389-403, 2008.

[44] A. S. Paula, K. K. Mahesh, C. M. L. dos Santos, F. M. Braz Fernandes, and C. S. da Costa Viana, "Thermomechanical behavior of Ti-rich NiTi shape memory alloys," *Materials Science and Engineering: A*, vol. 481–482, pp. 146-150, 2008.

[45] A. S. Paula, K. K. Mahesh, and F. M. Braz Fernandes, "Stability in Phase Transformation After Multiple Steps of Marforming in Ti-Rich Ni-Ti Shape Memory Alloy," *Journal of Materials Engineering and Performance*, vol. 20, pp. 771-775, 2011.

[46] Y. Motemani, M. Nili-Ahmadabadi, M. J. Tan, M. Bornapour, and S. Rayagan, "Effect of cooling rate on the phase transformation behavior and mechanical properties of Ni-rich NiTi shape memory alloy," *Journal of Alloys and Compounds*, vol. 469, pp. 164-168, 2009.

[47] B. Tam, M. I. Khan, and Y. Zhou, "Mechanical and Functional Properties of Laser-Welded Ti-55.8 Wt Pct Ni Nitinol Wires," *Metallurgical and Materials Transactions A*, vol. 42, pp. 2166-2175, 2011.

[48] A. Block-Bolten and T. W. Eagar, "Metal vaporization from weld pools," *Metallurgical Transactions B*, vol. 15, pp. 461-469, 1984.

[49] M. M. Collur, A. Paul, and T. Debroy, "Mechanism of alloying element vaporization during laser welding," *Metallurgical Transactions B*, vol. 18, pp. 733-740, 1987.

[50] M. Jandaghi, P. Parvin, M. J. Torkamany, and J. Sabbaghzadeh, "Alloying element losses in pulsed Nd : YAG laser welding of stainless steel 316," *Journal of Physics D: Applied Physics*, vol. 41, p. 235503, 2008.

[51] Y. T. Hsu, Y. R. Wang, S. K. Wu, and C. Chen, "Effect of CO2 laser welding on the shape-memory and corrosion characteristics of TiNi alloys," *Metallurgical and Materials Transactions A*, vol. 32, pp. 569-576, 2001.

[52] A. Pequegnat, M. Daly, J. Wang, Y. Zhou, and M. I. Khan, "Dynamic actuation of a novel laser-processed NiTi linear actuator," *Smart Materials and Structures*, vol. 21, p. 094004, 2012.

[53] C. Dawes, *Laser Welding*. New York, NY: McGraw-Hill, 1992.

[54] R.C. Crafer, P. J. Oakley, Ed., *Laser Processing in Manufacturing*. New York, NY: Chapman & Hall, 1993.

[55] S. S. Charschan, Ed., *Laser in Industry*. New York, NY: Van Nostrand Reinhold Company, 1972.

[56] E. Biro, "Weldability of Plated thin sheet and Cu by Pulsed Nd:YAG Laser welding," MASc Thesis, University of Waterloo, Waterloo, ON, Canada.

[57] W. W. Duley, *Laser Welding*: John Wiley & Sons, Inc. , 1999.

[58] R. N. Wright, *Wire technology process engineering and metallurgy*. Burlington, MA: Butterworth-Heinemann, 2011.

[59] B. Panton, "Laser Processing, Thermomechanical Processing, and Thermomechanical Fatigue of NiTi Shape Memory Alloys," PhD Thesis, Mechanical Engineering, University of Waterloo, Waterloo, ON, Canada, 2016.

[60] W. A. Backofen, "Deformation Processing," in *Anonymous Reading*, ed MA: Addison-Wesley Publishing Company, 1972, p. 139.

[61] R. N. Wright, "Physical Conditions in the Lubricant Layer," *Wire Journal International,* vol. 30, pp. 88-92, 1997.

[62] J. G. Wistreich, "THE FUNDAMENTALS OF WIRE DRAWING," *Metallurgical Reviews,* vol. 3, pp. 97-142, 1958.

[63] R. N. Wright, "Center bursts - A review of Criteria," in *2008 Conference Proceedings*, ed Guilford, CT: Wire Association International, Inc., 2008, p. 15.

[64] J. G. Wistreich, "Investigation of the Mechanics of Wire Drawing," in *Proceedings of the Institution of Mechanical Engineers*. vol. 169, ed, 1955, pp. 654-678.

[65] S. K. Wu, H. C. Lin, and Y. C. Yen, "A study on the wire drawing of TiNi shape memory alloys," *Materials Science and Engineering: A,* vol. 215, pp. 113-119, 1996/09/15 1996.

[66] R.N. Wright, A. T. Male, *ASME International, Journal for Lubrication Engineering, Series F*, vol. 97, p. 134, 1975.

[67] J. E. Schaffer and D. L. Plumley, "Fatigue Performance of Nitinol Round Wire with Varying Cold Work Reductions," *Journal of Materials Engineering and Performance,* vol. 18, pp. 563-568, 2009.

[68] D. A. Miller and D. C. Lagoudas, "Influence of cold work and heat treatment on the shape memory effect and plastic strain development of NiTi," *Materials Science and Engineering: A,* vol. 308, pp. 161-175, 2001.

[69] X. Lei, W. Rui, and L. Yong, "The optimization of annealing and cold-drawing in the manufacture of the Ni–Ti shape memory alloy ultra-thin wire," *The International Journal of Advanced Manufacturing Technology,* vol. 55, pp. 905-910, 2011.

[70] C. Grossmann, J. Frenzel, V. Sampath, T. Depka, A. Oppenkowski, C. Somsen, *et al.*, "Processing and property assessment of NiTi and NiTiCu shape memory actuator springs," *Materialwissenschaft und Werkstofftechnik,* vol. 39, pp. 499-510, 2008.

[71] S. K. Wu, H. C. Lin, Y. C. Yen, and J. C. Chen, "Wire drawing conducted in the R-phase of TiNi shape memory alloys," *Materials Letters,* vol. 46, pp. 175-180, 2000.

[72] K. Yamauchi, M. Nishida, I. Itai, K. Kitamura, and A. Chiba, "Specimen Preparation for Transmission Electron Microscopy of Twins in B19′ Martensite of Ti–Ni Shape Memory Alloys," *Materials Transactions, JIM,* vol. 37, pp. 210-217, 1996.

[73] Anonymous. (2006) Heat Treating...Putting the "Spring" in Springs. *Industrial Heating*. 24.

[74] P. R. N. Childs, "Chapter 15 - Springs," in *Mechanical Design Engineering Handbook*, ed Oxford: Butterworth-Heinemann, 2014, pp. 625-675.

[75] A. Spring, *Design handbook: engineering guide to spring design*. Bristol Conn.: Barnes Group Inc., 1987.

[76] L. Zebek. (2007) Understanding Spring Failures: Curvature Correction Factors. *SPRINGS*. 39-40.

[77] S. Ivana, "SPRINGS, THEIR DESIGN AND CALCULATIONS," in *Handbook of Die Design, Second Edition*, ed: McGraw Hill Professional, Access Engineering, 2006.

[78] K. Lingaiah, B. Iyengar, *Machine Design Handbook* vol. 1: Suma Publishers, 1986.

[79] A. S. Corporation, *Handbook of mechanical spring design*. Bristol, Conn., 1951.

[80] A. Paiva and M. A. Savi, "An overview of constitutive models for shape memory alloys," *Mathematical Problems in Engineering,* vol. 2006, p. 30, 2006.

[81] A. Menciassi, S. Gorini, G. Pernorio, and P. Dario, "A SMA actuated artificial earthworm," in *Robotics and Automation, 2004. Proceedings. ICRA '04. 2004 IEEE International Conference on*, 2004, pp. 3282-3287 Vol.4.

[82] K. Otsuka and C. M. Wayman, *Shape memory materials*: Cambridge university press, 1999.

[83] B. Kim, M. G. Lee, Y. P. Lee, Y. Kim, and G. Lee, "An earthworm-like micro robot using shape memory alloy actuator," *Sensors and Actuators A: Physical,* vol. 125, pp. 429-437, 2006.

[84] S. M. An, J. Ryu, M. Cho, and K.-J. Cho, "Engineering design framework for a shape memory alloy coil spring actuator using a static two-state model," *Smart Materials and Structures,* vol. 21, p. 055009, 2012.

[85] I. Czarnocki, W. Kim, B. Utter, J. Luntz, D. Brei, P. Alexander, "Design of SMA Helical Actuators: An Experimental Study," in *ASME 2013 Conference on Smart Materials, Adaptive Structures and Intelligent Systems*, Snowbird, Utah, USA, 2013.

[86] J. Zhang, D. Weckman, and Y. Zhou, "Effects of temporal pulse shaping on cracking susceptibility of 6061-T6 aluminum Nd: YAG laser welds," *WELDING JOURNAL-NEW YORK-*, vol. 87, p. 18, 2008.

[87] X. He, J. Norris, P. Fuerschbach, and T. DebRoy, "Liquid metal expulsion during laser spot welding of 304 stainless steel," *Journal of Physics D: Applied Physics*, vol. 39, p. 525, 2006.

[88] L. Corbin, "Dies & ceramics," in *Nonferrous Wire Handbook*, Anonymous, Ed., 3 ed Guildford, CT: The Wire Association,Inc., 1995, p. 477.

[89] A. Michael, Y. N. Zhou, and M. I. Khan, "Novel method to analyse tensile properties of ultra-fine NiTi wires with a visual extensometer," *Materials Letters*, vol. 182, pp. 177-180, 2016.

[90] T. Waitz, T. Antretter, F. D. Fischer, N. K. Simha, and H. P. Karnthaler, "Size effects on the martensitic phase transformation of NiTi nanograins," *Journal of the Mechanics and Physics of Solids*, vol. 55, pp. 419-444, 2007.

[91] T. Philip and P. A. Beck, "CsCl-type ordered structures in binary alloys of transition elements," *Trans AIME J Metals*, vol. 209, pp. 1269-1271, 1957.

[92] Y. Zheng, F. Jiang, L. Li, H. Yang, and Y. Liu, "Effect of ageing treatment on the transformation behaviour of Ti–50.9 at.% Ni alloy," *Acta Materialia*, vol. 56, pp. 736-745, 2008.

[93] Q. P. Sun and Y. HE, "A multiscale continuum model of the grain-size dependence of the stress hysteresis in shape memory alloy polycrystals," *International Journal of Solids and Structures*, vol. 45, 2008.

[94] L. Bataillard, J. E. Bidaux, and R. Gotthardt, "Interaction between microstructure and multiple-step transformation in binary NiTi alloys using in-situ transmission electron microscopy observations," *Philosophical Magazine A*, vol. 78, pp. 327-344, 1998.

[95] H. Morawiec, D. Stroz, and D. Chrobak, "Effect of deformation and thermal treatment of NiTi alloy on transition sequence," *Le Journal de Physique IV*, vol. 5, pp. C2-205-C2-210, 1995.